Monthly Notices
of the
ROYAL ASTRONOMICAL SOCIETY

MNRAS **463,** 3921–3947 (2016)
Advance Access publication 2016 September 8

doi:10.1093/mnras/stw2267

Instability of supersonic cold streams feeding galaxies – I. Linear Kelvin–Helmholtz instability with body modes

Nir Mandelker,[1★] Dan Padnos,[1★] Avishai Dekel,[1★] Yuval Birnboim,[1]
Andreas Burkert,[2,3] Mark R. Krumholz[4,5] and Elad Steinberg[1]

[1]*Centre for Astrophysics and Planetary Science, Racah Institute of Physics, The Hebrew University, Jerusalem 91904, Israel*
[2]*Unitversitäts-Sternwarte München, Scheinerstr. 1, D-81679 Munich, Germany*
[3]*Max Planck Institute for Extraterrestrial Physics, Giessenbachstr. 1, D-85748 Garching, Germany*
[4]*Department of Astronomy and Astrophysics, University of California, Santa Cruz, CA 95064, USA*
[5]*Research School of Astronomy & Astrophysics, Australian National University, Cotter Road, Weston, ACT 2611, Australia*

Accepted 2016 September 6. Received 2016 September 6; in original form 2016 June 20

ABSTRACT

Massive galaxies at high redshift are predicted to be fed from the cosmic web by narrow, dense streams of cold gas that penetrate through the hot medium encompassed by a stable shock near the virial radius of the dark-matter halo. Our long-term goal is to explore the heating and dissipation rate of the streams and their fragmentation and possible breakup, in order to understand how galaxies are fed, and how this affects their star formation rate and morphology. We present here the first step, where we analyse the linear Kelvin–Helmholtz instability (KHI) of a cold, dense slab or cylinder in 3D flowing supersonically through a hot, dilute medium. The current analysis is limited to the adiabatic case with no gravity. By analytically solving the linear dispersion relation, we find a transition from a dominance of the familiar rapidly growing *surface* modes in the subsonic regime to more slowly growing *body* modes in the supersonic regime. The system is parametrized by three parameters: the density contrast between stream and medium, the Mach number of stream velocity with respect to the medium and the stream width with respect to the halo virial radius. A realistic choice for these parameters places the streams near the mode transition, with the KHI exponential-growth time in the range 0.01–10 virial crossing times for a perturbation wavelength comparable to the stream width. We confirm our analytic predictions with idealized hydrodynamical simulations. Our linear estimates thus indicate that KHI may be effective in the evolution of streams before they reach the galaxy. More definite conclusions await the extension of the analysis to the non-linear regime and the inclusion of cooling, thermal conduction, the halo potential well, self-gravity and magnetic fields.

Key words: hydrodynamics – instabilities – galaxies: evolution – galaxies: formation.

1 INTRODUCTION

According to the standard Λ cold dark matter model of cosmology, the most massive haloes at any epoch lie at the nodes of the cosmic web, and are penetrated by cosmic filaments of dark matter (e.g. Bond, Kofman & Pogosyan 1996; Springel et al. 2005; Dekel et al. 2009). These represent high-sigma peaks in the density fluctuation field, much more massive than the Press–Schechter mass, M_*, of typical haloes at that time (Press & Schechter 1974). At redshift $z = 1$–4, when star formation is at its peak and most of the mass is assembled into galaxies (Madau, Pozzetti & Dickinson 1998; Hopkins & Beacom 2006; Madau & Dickinson 2014), such haloes have virial masses of $M_{\rm v} \sim 10^{12}\,{\rm M}_\odot$ and above, larger than the critical mass for shock heating $M_{\rm shock} \lesssim 10^{12}\,{\rm M}_\odot$ (Birnboim & Dekel 2003; Dekel & Birnboim 2006). They thus contain hot gas at the virial temperature, $T_{\rm v} \sim 10^6$ K. However, for such high-sigma peaks, the filaments that feed the halo are significantly narrower than the virial radius, and the gas residing in them is much denser than the halo gas. Therefore, the radiative cooling time of the stream gas is shorter than the local compression time, preventing the formation of a stable virial shock within the streams. The streams are thus expected to remain cold, with temperatures of $T_{\rm s} \gtrsim 10^4$ K, allowing them to penetrate efficiently through the hot halo circumgalactic medium (CGM) on to the central galaxy (Dekel & Birnboim 2006).

The above theoretical picture is supported by cosmological simulations (Kereš et al. 2005; Ocvirk, Pichon & Teyssier 2008; Dekel et al. 2009; Ceverino, Dekel & Bournaud 2010; Faucher-Giguère,

★E-mail: nir.mandelker@mail.huji.ac.il (NM); dan.padnos@mail.huji.ac.il (DP); avishai.dekel@mail.huji.ac.il (AD)

Kereš & Ma 2011; van de Voort et al. 2011). In these simulations, cold streams with widths of a few to 10 per cent of the virial radius penetrate deep into the halo. This gas supply allows the high star formation rates (SFRs) of $\sim 20-200\,\mathrm{M}_\odot\,\mathrm{yr}^{-1}$ observed in massive star-forming galaxies (SFGs) with baryonic masses of $\sim 10^{11}\,\mathrm{M}_\odot$ at $z \sim 2$ (Förster Schreiber et al. 2006; Genzel et al. 2006, 2008; Elmegreen et al. 2007; Stark et al. 2008). These high SFR values are only a factor of $\lesssim 2$ lower than the accretion rate at the virial radius, implying that at least half the gas mass flux brought into the halo by the streams must reach the central galaxy (Dekel et al. 2009), irrespective of what happens to the stream structure and thermal properties along the way. The streams also play a key role in the buildup of angular momentum in disc galaxies (Kimm et al. 2011; Pichon et al. 2011; Stewart et al. 2011, 2013; Codis et al. 2012; Danovich et al. 2012, 2015).

Cosmological simulations indicate that the streams maintain roughly constant inflow velocities as they travel from the outer halo to the central galaxy (Dekel et al. 2009; Goerdt & Ceverino 2015). The constant velocity, as opposed to the expected gravitational acceleration, indicates energy loss into radiation which may be observed as Lyman α cooling emission (Dijkstra & Loeb 2009; Faucher-Giguère et al. 2010; Goerdt et al. 2010), though the dissipation process has not been explored yet. Based on radiative transfer models, the total luminosity and the spatial structure of the emitted radiation appear similar to Lyman α 'blobs' observed at $z > 2$ (Steidel et al. 2000; Matsuda et al. 2006, 2011). The models find that roughly half the radiation comes from the dissipation of gravitational energy while the other half is due to heating from the UV background (Goerdt et al. 2010, though see also Faucher-Giguère et al. 2010 who found somewhat lower luminosities in their simulations). Radiative transfer models also show that a central quasar can power the emission by supplying seed photons which scatter inelastically within the filaments, producing Lyman α cooling emission that extends to several hundred kpc and appears similar to observed structures (Cantalupo et al. 2014). Recent observations using the MUSE integral-field instrument suggest that such extended Lyman α emitting nebulae are ubiquitous around the brightest quasars at $z \sim 3.5$ (Borisova et al. 2016). In addition to emission, the cold streams consisting of mostly neutral hydrogen should also be visible in absorption, and can account for observed Lyman-limit systems and damped Lyman α systems (Fumagalli et al. 2011; Goerdt et al. 2012; van de Voort et al. 2012). Observations using absorption features along quasar sightlines to probe the CGM of massive SFGs at $z \sim 1$–2 reveal low-metallicity, coplanar, corotating accreting material (Bouché et al. 2013, 2016; Prochaska, Lau & Hennawi 2014), providing further observational support for the cold-stream paradigm. Strong Lyman α absorption has also been detected in the CGM of massive sub-millimetre galaxies at $z \sim 2$ (Fu et al. 2016).

Despite the growing evidence from simulations and observations that cold streams are a fundamental part of galaxy formation at high redshift, several important questions remain regarding their evolution. How much of the stream energy is dissipated as they travel through the CGM? What are the implications on the emitted radiation and the mass inflow rate on to the galaxy? How do the streams join the galaxy, in terms of coherency versus fragmentation/clumpiness, temperature and velocity? How does this affect the growth of angular momentum and the SFR in the disc?

While there is some preliminary observational evidence for the fragmentation of cold streams (Cantalupo et al. 2014), most attempts to address these questions have used cosmological simulations. Unfortunately, in current cosmological simulations, the resolution within the streams is never better than a few hundred pc, and is often of the order of a kpc, comparable to the stream width itself. They thus cannot resolve the detailed physical processes associated with stream instabilities necessary to properly address these questions. Grid-based adaptive-mesh-refinement (AMR) codes show streams that remain cold and coherent outside of $\sim 0.3R_\mathrm{v}$, inside of which a messy interaction region is seen where the streams collide, fragment and experience strong torques before settling on to the disc (Ceverino et al. 2010; Danovich et al. 2015). These simulations exhibit high gas mass accretion rates on to the central galaxy, roughly half the virial accretion rate (Dekel et al. 2013). Simulations using the moving mesh code AREPO (Springel 2010; Vogelsberger et al. 2012) suggest that the streams heat up at ~ 0.25–$0.5R_\mathrm{v}$, with most of the accreted gas heating to roughly the virial temperature before falling on to the galaxy (Nelson et al. 2013). Nevertheless, the mass inflow rate on to the central galaxy ends up very similar to the virial accretion rate, likely because the dense stream gas in the inner halo rapidly cools after heating. It is unclear whether this gas is ever in hydrostatic equilibrium within the halo. The same study argued that previous reports of streams remaining cold and coherent in smoothed-particle-hydrodynamic (SPH) simulations were due to numerical inaccuracies associated with the standard formulation of SPH.

Since current cosmological simulations are far from being able to properly resolve the streams, a more fundamental analytical and numerical approach is warranted. The physical problem of the evolution of a supersonic, cold, dense, gas stream in a hot, dilute medium has not been addressed thus far in the literature, even at its simplest hydrodynamic level of Kelvin–Helmholtz instability (KHI).[1] This is the first in a series of papers where we study this issue, in the context of cold streams feeding massive galaxies at high redshift, using analytic models of increasing complexity together with idealized simulations and concluding with full-scale cosmological simulations with tailored mesh refinement in the streams.

In this paper, we take the first step and address KHI under fully compressible conditions.[2] We derive the dispersion relation for the growth of linear instabilities in a confined planar slab and cylinder, and ask whether such instabilities grow to non-linear amplitudes in a virial crossing time. In a forthcoming paper (Padnos et al., in preparation), we will address in detail, analytically and using idealized simulations, the non-linear evolution of these instabilities. In future work, we will add one by one thermal conduction, cooling, the external potential of the host halo, self-gravity and magnetic fields. In the final phase, we will study cosmological simulations with forced mesh refinement in the streams, to explore the effect of stream instability on galaxy formation at the halo centre and the effects of feedback on the streams.

This paper is organized as follows. In Section 2, we summarize the derivation of the linear dispersion relation for compressible KHI in different idealized geometries. Mathematical details of the derivations are provided in several appendices, which may be of interest to the mathematically inclined reader. In Section 3, we use numerical simulations to test the analytic predictions of the preceding section. In Section 4, we apply the analytic formalism

[1] The problem of a hot jet travelling supersonically in a cold medium has been studied, see references in Section 2.

[2] We use 'compressible' to refer to flows with arbitrary Mach number, supersonic ($M > 1$), transonic ($M \sim 1$) or subsonic ($M < 1$). We use 'incompressible' to refer to the limit where $M \to 0$, equivalent to taking the sound speed $c \to \infty$. Since pressure and density are related through the sound speed, $\mathrm{d}P \propto c^2 \mathrm{d}\rho$, the density is effectively constant in the incompressible limit.

to the case of cosmic cold streams and estimate the number of e-foldings of growth experienced by initially small perturbations within a virial crossing time. In Section 5, we speculate as to the effects of additional physics not included in our analysis, presenting an outline for future work. We discuss our results and summarize our conclusions in Section 6.

2 COMPRESSIBLE KHI

In this section, we derive the dispersion relations for compressible KHI in several different geometries. For simplicity and analytic tractability, we begin by deriving the relation in planar geometry, first discussing a 'two-zone instability', or a *sheet*, where two semi-infinite fluids are separated by a single planar interface, and then a 'three-zone instability', or a *slab*, where one fluid is confined to a planar slab of finite thickness and surrounded by a second (background) fluid from both sides. KHI in a slab is qualitatively different than in a sheet due to the appearance of *body modes*, unstable perturbations caused by waves reverberating back and forth between the slab boundaries, that dominate the instability at high Mach numbers (Section 2.3.4). We then derive the dispersion relation for a cylindrical stream, and show that the behaviour of linear perturbations with wavelengths comparable to or smaller than the stream radius is effectively identical to that of perturbations in a slab.

Several previous studies have addressed linear stability of astrophysical jets to KHI in both planar and cylindrical geometries, both analytically and numerically (e.g. Ferrari, Trussoni & Zaninetti 1978; Birkinshaw 1984, 1990; Payne & Cohn 1985; Hardee 1987; Hardee & Norman 1988; Norman & Hardee 1988; Bodo et al. 1994; Perucho et al. 2004). These studies focus primarily on hot, dilute jets travelling in cold, dense media. As we will see below, the main difference between such a scenario and that studied here, of cold streams in a hot medium, is the ratio of the stream sound-crossing time to the KHI exponential-growth time. While this can be important for the overall stability of the stream (see Section 4), it does not fundamentally alter the linear dispersion relation, and our derivation is similar to those presented in Payne & Cohn (1985, for the cylinder) and Hardee & Norman (1988, for the slab). However, there are certain differences in our approaches and conclusions which we highlight in the text, and we find our analysis to be more complete, addressing a sheet, a slab and a cylinder in a self-contained and consistent way.

2.1 General KHI in planar coordinates

We begin with the basic equations of hydrodynamics, which represent conservation of mass (the continuity equation), momentum (the Euler equation) and energy:

$$\frac{\partial \rho}{\partial t} + (\boldsymbol{v}\cdot\nabla)\,\rho + \rho\nabla\cdot\boldsymbol{v} = 0, \tag{1}$$

$$\rho\left[\frac{\partial \boldsymbol{v}}{\partial t} + (\boldsymbol{v}\cdot\nabla)\,\boldsymbol{v}\right] + \nabla P = 0, \tag{2}$$

$$\frac{\partial P}{\partial t} + (\boldsymbol{v}\cdot\nabla)\,P - c^2\left[\frac{\partial \rho}{\partial t} + (\boldsymbol{v}\cdot\nabla)\,\rho\right] = 0. \tag{3}$$

Above, ρ is the fluid's density, $\boldsymbol{v}$ its velocity and P the pressure in the fluid. We assume an ideal equation of state, so $c = (\gamma P/\rho)^{1/2}$ is the sound speed, where γ is the adiabatic index of the fluid, $\gamma = (\partial \ln P/\partial \ln\rho)_s$.

We consider a time-independent flow in the $\hat{z}$ direction, where the flow velocity and the fluid density are arbitrary functions of x (in Cartesian coordinates):

$$\rho_0(x,y,z) = \rho_0(x), \quad \boldsymbol{v}_0(x,y,z) = v_0(x)\hat{z}. \tag{4}$$

In this case, with no external forces, equation (2) dictates that the pressure is uniform, $P_0(x,y,z) = P_0$. On top of this equilibrium flow, we impose small perturbations in the fluid variables, $\rho = \rho_0 + \rho_1$, $\boldsymbol{v} = v_0\hat{z} + \boldsymbol{u}$ and $P = P_0 + P_1$, where the perturbation in each variable f obeys $f_1 \ll f_0$. To study the growth of instabilities, we decompose each of the perturbed quantities into Fourier modes of the form

$$f_1(x,y,z,t) = f_1(x)\mathrm{e}^{\mathrm{i}(k_y y + k_z z - \omega t)}. \tag{5}$$

In other words, the perturbations are travelling waves in the yz plane with wave vector $\boldsymbol{k} = k_y\hat{y} + k_z\hat{z}$ and frequency ω and an arbitrary x dependence.

By inserting these perturbations into equations (1)–(3) and linearizing, we can derive algebraic relations between the x-dependent amplitudes of the pressure perturbation and its derivatives with respect to x to those of all other perturbations.[3] Using the conventions $\partial f/\partial x = f'$, $k_z = k\cos(\varphi)$, $k_y = k\sin(\varphi)$ and $v_k = \boldsymbol{v}_0\cdot\hat{\boldsymbol{k}} = v_0\cos(\varphi)$, we obtain

$$\rho_1 = -\frac{1}{k^2\left(v_k - \frac{\omega}{k}\right)^2}\left[P_1'' - \frac{2v_k'}{v_k - \frac{\omega}{k}}P_1' - k^2 P_1\right], \tag{6}$$

$$u_z = -\frac{\cos(\varphi)}{\rho_0\left(v_k - \frac{\omega}{k}\right)}\left[\frac{v_k'}{k^2\cos^2(\varphi)\left(v_k - \frac{\omega}{k}\right)}P_1' + P_1\right], \tag{7}$$

$$u_y = -\frac{\sin(\varphi)}{\rho_0\left(v_k - \frac{\omega}{k}\right)}P_1, \tag{8}$$

$$u_x = \frac{\mathrm{i}}{\rho_0 k\left(v_k - \frac{\omega}{k}\right)}P_1'. \tag{9}$$

Note that in equations (6)–(9) all fluid variables are functions of x. In addition, we are left with a second-order ordinary differential equation (ODE) for $P_1(x)$:

$$P_1'' - \left[\frac{2v_k'}{v_k - \frac{\omega}{k}} + \frac{\rho_0'}{\rho_0}\right]P_1' - k^2\left[1 - \left(\frac{v_k - \frac{\omega}{k}}{c}\right)^2\right]P_1 = 0. \tag{10}$$

Equation (10) is an eigenvalue equation. Given profiles along x for the unperturbed density and velocity and boundary conditions for P_1, solutions exist only for certain combinations of ω and k, which define the dispersion relation, $\omega(k)$. Since equation (10) depends only on the component of the velocity parallel to the perturbation wave vector, v_k, with no explicit dependence on the propagation angle φ, we restrict our analysis to perturbations where $k_y = 0$ so that $v_k = v_0$.

2.1.1 *Temporal versus spatial stability analysis*

There are in general two types of stability analyses, *temporal* and *spatial*. In the former, the wavenumber k is real while the frequency ω is complex. Physically, this represents seeding the entire system with a *spatially oscillating* perturbation and studying its *temporal*

[3] We could have chosen any of the five perturbed variables and expressed the other four in terms of it. However, the pressure is a convenient choice because it must always be continuous, while the other variables can in principle have discontinuities.

growth. In the latter, ω is real while k is complex. This represents seeding a *temporally oscillating* perturbation at the stream origin and studying its downstream *spatial growth*. This distinction is particularly important when performing numerical simulations, as they change the required boundary and initial conditions. Studies of the stability of jets whose source has intrinsic variability (such as an AGN or a gamma-ray burst) often employ spatial stability analyses. However, the cosmic web streams we are studying do not have a well-defined variable source outside the halo, but rather experience perturbations from the halo throughout their extent. Therefore, we perform a temporal stability analysis, envisioning a stationary stream suffering some perturbation across its extent, and asking how much the perturbation will grow in a virial crossing time.

2.2 The planar sheet

We first consider the classic case of two fluids separated at $x = 0$. For consistency with later sections when we discuss a confined *stream* with finite thickness in a *background*, we label the two fluids with subscripts 'b' and 's', for $x > 0$ and $x < 0$, respectively. We assume each fluid to have initially uniform density and velocity. This problem is often referred to as the 'vortex sheet' and was first addressed for two compressible fluids by Landau (1944). In this case, the second term in equation (10) vanishes for all $x \neq 0$. The equation must be solved separately in the regions $x > 0$ and $x < 0$, subject to the boundary conditions that the pressure perturbation vanishes at infinity and is continuous across the boundary at $x = 0$. The solution is

$$P_1 = \begin{cases} A\mathrm{e}^{-q_\mathrm{b} x} & x > 0 \\ A\mathrm{e}^{q_\mathrm{s} x} & x < 0 \end{cases}, \tag{11}$$

where A is a constant of integration that depends on the initial conditions, and we have defined the generalized wavenumbers q_b and q_s by

$$q_\mathrm{b,s} = k\left[1 - \left(\frac{\omega - k v_\mathrm{b,s}}{k c_\mathrm{b,s}}\right)^2\right]^{1/2}. \tag{12}$$

Since ω is in general complex, $q_\mathrm{b,\,s}$ is the square root of a complex number, forcing us to choose a branch cut in the complex plane. We have chosen to define $\mathrm{Re}(q_\mathrm{b,\,s}) > 0$, which ensures that the amplitude of perturbations decays exponentially away from the interface between the two fluids. These are therefore known as 'surface modes'. A somewhat technical discussion of the meaning and justification of this branch cut can be found in Appendix A.

To proceed, we require a fourth boundary condition. This is achieved by realizing that the velocity perpendicular to the interface between the fluids causes a spatial displacement in the interface position, from $x = 0$ to h, and this displacement must be the same when approaching the interface from either side. This is often called 'the Landau condition'. Expanding h in the same Fourier modes as the other perturbed quantities, this results in the first-order equation

$$u_x|_{x=0} = \frac{\partial h}{\partial t} + (\boldsymbol{v}\cdot\nabla)h = \mathrm{i}k\left(v_0|_{x=0} - \frac{\omega}{k}\right)h. \tag{13}$$

Inserting equations (9) and (11) into (13) from both sides of the interface and then dividing out h yields the dispersion relation

$$\frac{(\omega - k v_\mathrm{b})^2}{(\omega - k v_\mathrm{s})^2} = -\frac{\rho_\mathrm{s}}{\rho_\mathrm{b}}\frac{q_\mathrm{b}}{q_\mathrm{s}}. \tag{14}$$

In the incompressible limit, the speed of sound goes to infinity in both media, and therefore from equation (12) $q_\mathrm{b,\,s} \to k$. In this limit, equation (14) reduces to the familiar form of the classical Kelvin–Helmholtz dispersion relation (e.g. Chandrasekhar 1961)

$$\omega_\pm = \frac{\rho_\mathrm{b} v_\mathrm{b} + \rho_\mathrm{s} v_\mathrm{s}}{\rho_\mathrm{b} + \rho_\mathrm{s}}k \pm \mathrm{i}\frac{\sqrt{\rho_\mathrm{s}\rho_\mathrm{b}}|v_\mathrm{s} - v_\mathrm{b}|}{\rho_\mathrm{b} + \rho_\mathrm{s}}k. \tag{15}$$

Since the growth rate cannot depend on the frame of reference, we analyse the general case in the frame where the background is static, $v_\mathrm{b} = 0$, and the stream is moving with velocity $v_\mathrm{s} = v$. Furthermore, we define unitless variables

$$\varpi \equiv \frac{\omega}{kV}, \qquad \delta \equiv \frac{\rho_\mathrm{s}}{\rho_\mathrm{b}}, \qquad M_\mathrm{b,s} \equiv \frac{V}{c_\mathrm{b,s}}. \tag{16}$$

Here, ϖ is the phase velocity in units of the stream velocity, δ is the density contrast between the stream and the background and $M_\mathrm{b,\,s}$ are the Mach number of the stream velocity with respect to the background and the stream itself, respectively. Since pressure equilibrium is assumed, $M_\mathrm{s} = \sqrt{\delta}M_\mathrm{b}$. In this notation, the dispersion relation for the incompressible sheet, equation (15), becomes

$$\varpi_\pm = \frac{\delta}{1+\delta} \pm \mathrm{i}\frac{\delta^{1/2}}{1+\delta}. \tag{17}$$

By further defining

$$Z \equiv -\frac{1}{\delta}\left(\frac{\varpi}{\varpi - 1}\right)^2\left(\frac{1 - \delta M_\mathrm{b}^2(\varpi - 1)^2}{1 - M_\mathrm{b}^2\varpi^2}\right)^{1/2}, \tag{18}$$

the dispersion relation for the compressible sheet, equation (14), becomes

$$Z = 1, \tag{19}$$

an algebraic equation for the unknown ϖ. We learn from the equation that ϖ depends only on δ and M_b, with no dependence on k. This implies that $\omega \propto Vk$, which could have been predicted from dimensional analysis, since the only length-scale in the problem is the perturbation wavelength.

By squaring both sides of equation (19), inserting equation (18) and rearranging, we get a sixth-degree polynomial equation in ϖ that can be factored as the product of a quadratic with a quartic

$$\left[\delta(\varpi - 1)^2 - \varpi^2\right]\cdot\left[\delta(\varpi - 1)^2\left(M_\mathrm{b}^2\varpi^2 - 1\right) - \varpi^2\right] = 0. \tag{20}$$

A detailed analysis of this equation is presented in Appendix B. We summarize the main points below. The two roots of the quadratic part and two of the four roots of the quartic part are always real, and do not solve equation (19). Rather they are solutions to the equation $Z = -1$, arising from the fact that we squared equation (19). At low Mach numbers, the two remaining roots of the quartic part are complex conjugates, representing a growing unstable mode and a decaying mode. Both of these are indeed solutions to equation (19), with $Z = 1$. Equation (19) thus admits only two solutions, a growing and a decaying mode, as in the incompressible limit (equation 17). However, above a critical Mach number, these two complex roots become real as well (while still solving $Z = 1$), and the dispersion relation admits only *stable* solutions. For $M_\mathrm{b} \gg 1$, the solutions converge to

$$\varpi_\infty = M_\mathrm{b}^{-1},\ 1 - M_\mathrm{s}^{-1}, \tag{21}$$

which represent waves with phase velocities $\omega/k = c_\mathrm{b}, v - c_\mathrm{s}$.

The critical Mach number for stability is given by

$$M_\mathrm{crit} = \left(1 + \delta^{-1/3}\right)^{3/2}. \tag{22}$$

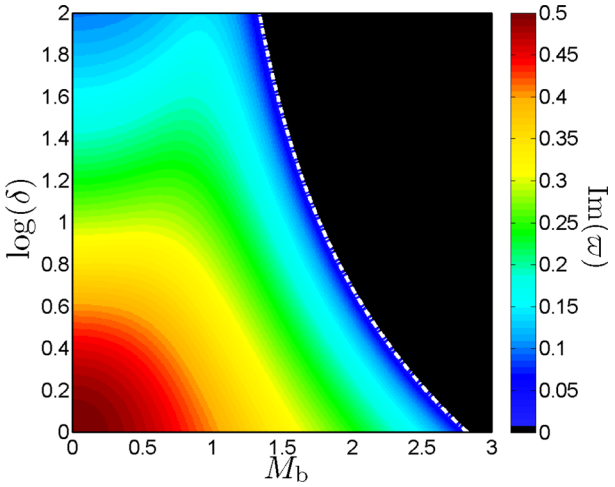

Figure 1. Growth rate for unstable modes of the sheet as a function of the Mach number, M_b, and the density contrast, δ. Colour represents the imaginary part of $\varpi = \omega/(kV)$. The black region at high Mach numbers shows the stable zone where linear perturbations do not grow. The white dash–dotted line shows the analytic expression for M_{crit}, the critical Mach number above which the sheet is stable, given by equation (22).

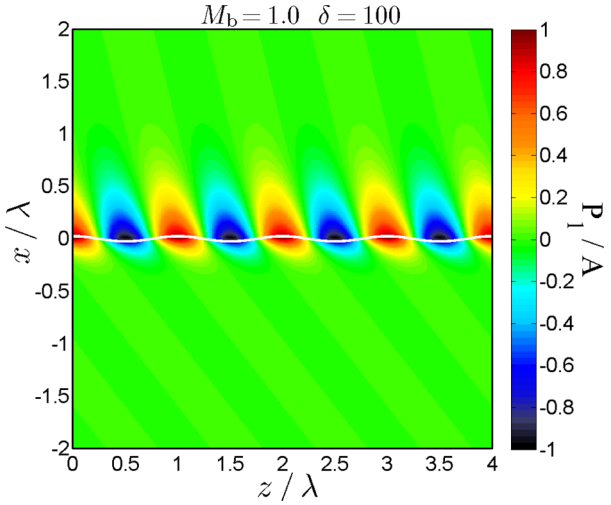

Figure 2. Pressure perturbation in a sheet with $M_b = 1.0$ and $\delta = 100$, from equation (11), with the dense fluid on the bottom. The white line represents the perturbation in the interface height, which has an amplitude of $h = 0.025\lambda$. This is a *surface mode*, which decays exponentially with distance from the interface, because $q_{b,s}$ are nearly real. The wave penetrates deeper into the fluid with lower density, and the angle of wave propagation breaks at the interface between the fluids.

This generalizes the result of Landau (1944), who showed that for identical fluids, with $\delta = 1$, the flow is stable above $M_{crit} = \sqrt{8} \simeq 2.83$. For $\delta = 10$ and 100, $M_{crit} \sim 1.77$ and 1.34, respectively.

The analytic expression for the growing mode solution as a function of M_b and δ can be found by finding the roots of the quartic polynomial in equation (20) and picking the complex root with the positive imaginary part. However, the full expression is very long and intractable. We show the growth rate of the instability, $\mathrm{Im}(\varpi)$, as a function of M_b and δ in Fig. 1. As $M_b \to 0$, the growth rate converges to the solution for an incompressible sheet (equation 17). For fixed δ, raising M_b from 0 to a relatively small value causes the growth rate to become larger, meaning the system becomes more unstable. However, raising M_b further to larger values causes the growth rate to decline, until it reaches zero at M_{crit}, shown by the white curve.

Some intuition as to why the sheet becomes stable to linear perturbations at high Mach numbers can be gained by considering what happens when the initially flat interface is perturbed with a sinusoidal displacement. Upstream of each 'crest', the fluids are set to collide, creating a high-pressure area, while downstream the fluids are set to separate, creating a low-pressure area (see Fig. 2). The flow that develops in response to this pressure perturbation tends to increase the perturbation amplitude. The typical time-scale for this process to occur is the sonic time across a perturbation wavelength, λ/c. However, if the flow is sufficiently fast with a high Mach number, this becomes very long compared to the relevant time-scale for the steady state flow, λ/v. In this case, the fluid upstream does not have time to react to the displacement of the interface, colliding with the crests rather than flowing around them and suppressing the instability.

By inserting the growing mode solution into equation (12) and then into equation (11), we obtain the spatial form of the pressure perturbation. This is shown in Fig. 2 for the case $M_b = 1.0$ and $\delta = 100$. We have normalized the perturbation by its maximum amplitude A, so that it is unity at $x = 0$. For reference, we also show the expected form of the perturbed interface, with an amplitude $h = 0.025\lambda$, where λ is the perturbation wavelength. The pressure perturbation decays rapidly with distance from the interface because $q_{b,s}$ are nearly real. This is a general feature of *surface modes*. The differences in penetration depth and propagation angle between the two fluids are caused by differences in the real and imaginary parts of q respectively between the two fluids. In the language of acoustic waves, this is caused by a change in the acoustic impedance of the two fluids.

2.3 The planar slab

We now consider a three-zone problem, which we refer to as the *slab*. The slab is confined to the region $|x| < R_s$ and is infinite in the y and z directions. We refer to the fluid at $|x| > R_s$ as the background, and assume it to be the same fluid on either side of the slab. As before, we assume each unperturbed medium to have uniform density and velocity. Following the same procedure as in Section 2.2, we solve equation (10) in each region subject to the boundary conditions that P_1 vanishes at infinity and is continuous across both slab interfaces. The result is

$$P_1 = \begin{cases} A\, \mathrm{e}^{-q_b(x-R_s)} & x > R_s \\ \frac{A\, \sinh(q_s[x+R_s]) - D\, \sinh(q_s[x-R_s])}{\sinh(2q_s R_s)} & |x| < R_s \\ D\, \mathrm{e}^{q_b(x+R_s)} & x < -R_s \end{cases}, \quad (23)$$

where A and D are two constants of integration.

By applying the Landau condition (equation 13) at the interfaces, $x = \pm R_s$, we learn that they are not independent. A self-consistent solution where both A and D are non-zero requires $A = \pm D$, which in turn gives a relationship between the displacement of the two interfaces from equilibrium $h_{R_s} = \mp h_{-R_s}$. The case $A = D$, $h_{R_s} = -h_{-R_s}$ corresponds to a symmetric perturbation of the pressure and is called the *pinch mode*, hereafter P-mode. The other case corresponds to an antisymmetric perturbation of the pressure and is called the *sinusoidal mode*, hereafter S-mode. These are shown schematically in Fig. 3.

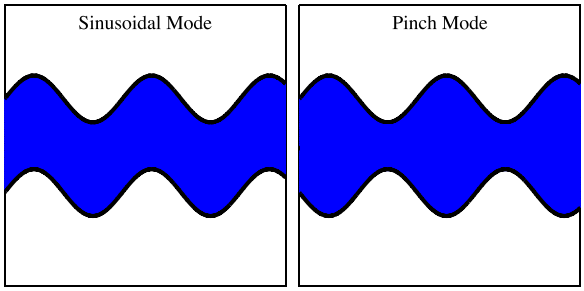

Figure 3. Schematic representation of the two instability modes in the planar slab. The left-hand panel represents the antisymmetric S-mode while the right-hand panel represents the symmetric P-mode.

Inserting these two solutions into equation (23) gives for the pressure perturbation within the slab

$$P_{1,s}(x) = A\,\frac{S(q_s x)}{S(q_s R_s)}, \tag{24}$$

where $S(x) = \sinh(x)$ or $\cosh(x)$ for S-modes or P-modes, respectively. The corresponding dispersion relations are

$$\frac{(\omega - k v_b)^2}{(\omega - k v_s)^2} = -\frac{\rho_s}{\rho_b}\frac{q_b}{q_s} T(q_s R_s), \tag{25}$$

where $T(x) = \tanh(x)$ or $\coth(x)$ for S-modes or P-modes, respectively.

To simplify equation (25), we again move into the frame where the background is static and the slab velocity is $v_s = v$, and rewrite the equation in unitless form, using equation (16) and

$$K = k R_s. \tag{26}$$

The result is

$$Z = T\left(\left[1 - \delta M_b^2 (\varpi - 1)^2\right]^{0.5} K\right), \tag{27}$$

where Z is defined in equation (18). This should be compared to the dispersion relation for the sheet, $Z = 1$.

The dispersion relations for S- and P-modes can be written as a single equation by inverting equation (27) and writing K as a function of ϖ,

$$K = 0.5\left[1 - \delta M_b^2 (\varpi - 1)^2\right]^{-0.5}(\alpha + \mathrm{i}\beta) \tag{28a}$$

$$\alpha = \ln(|1 + Z|) - \ln(|1 - Z|) \tag{28b}$$

$$\beta = \arg(1 + Z) - \arg(1 - Z) + n\pi, \tag{28c}$$

where n is any whole number, odd for P-modes and even for S-modes, and $\arg(1 \pm Z)$ is between $-\pi$ and π due to our chosen branch cut (see Appendix A).

Equations (25), (27) and (28) can be used interchangeably as the dispersion relation for the compressible slab. From equations (28), we learn that the slab solutions exhibit a qualitatively different behaviour than the sheet, for two reasons. First, in the sheet, ϖ was independent of k which resulted in the scaling $\omega \propto k$. On the other hand, in the slab, ϖ depends explicitly on K. This is due to the additional length-scale in the problem, the slab width, and will lead to a non-trivial dependence of the growth rate on wavenumber. Secondly, while equation (14) admitted only one solution for the growing mode $\omega(k)$, in slab geometry there can be an infinite number of modes for a fixed wavenumber k, each corresponding to a different value of n in equations (28), arising from the periodicity of tanh for complex arguments. We will discuss this in detail in the following sections, where we begin by examining various limits of the dispersion relation.

2.3.1 *Incompressible limit*

In the incompressible limit, when in equation (12) $q_{b,s} \to k$, the slab dispersion relation, equation (25), reduces to

$$\omega_\pm = \frac{\rho_b v_b + T(K)\rho_s v_s}{\rho_b + T(K)\rho_s} k \pm \mathrm{i}\frac{\sqrt{T(K)\rho_s\rho_b}|v_s - v_b|}{\rho_b + T(K)\rho_s} k. \tag{29}$$

It is straightforward to see that this converges to equation (15) for short wavelengths, $K \gg 1$. In practice, convergence is achieved for wavelengths $\lambda \lesssim 3R_s$. At long wavelengths, $K \ll 1$, both modes have $\omega \propto k^{1.5}$, meaning that the growth rate for the slab decays more rapidly than for the sheet as $k \to 0$. The dashed lines in Fig. 4 show the growth rates ($\mathrm{Im}(\omega)$, left) and oscillation frequencies ($\mathrm{Re}(\omega)$, right) as a function of K for the incompressible slab with $\delta = 100$, in comparison to the compressible slab discussed below.

2.3.2 *Long-wavelength limit*

In the long-wavelength limit, as $K \to 0$, we show in Appendix C that $q_{b,s} \to 0$ as well. Therefore, $\tanh(q_s R_s) \simeq 1/\coth(q_s R_s) \simeq q_s R_s$. This can be used to simplify equation (27) and expand ϖ in a power series in K. The result is that both S- and P-modes are unstable at long wavelengths for any M_b and δ. For this reason, the long-wavelength modes are referred to as *fundamental modes*. To leading order in K, the dispersion relations for the S- and P-modes are (see Appendix C for the derivation)

$$\varpi_{S,f} \simeq \delta K \pm \mathrm{i}(\delta K)^{1/2}\ (\mathrm{S}), \tag{30a}$$

$$\varpi_{P,f} \simeq 1 \pm \mathrm{i}\delta^{-1/2}(1 - M_b^2)^{-1/4} K^{1/2}\ (\mathrm{P}). \tag{30b}$$

As $K \to 0$, the fundamental S- and P-modes approach $\varpi = 0$ and 1, respectively, which result in $(1 + Z)/(1 - Z) = 1$ and -1. These modes thus correspond to $n = 0$ and -1 in equation (28).

It is instructive to compare these solutions to the long-wavelength limit of the incompressible slab (equation 29). To leading order in K, the fundamental S-mode is identical to the incompressible case. Corrections dependent on Mach number are all higher order in K. On the other hand, the growth rate of the fundamental P-mode is multiplied by a factor[4] $(1 - M_b^2)^{-1/4}$ compared to the incompressible case. For $M_b \ll 1$, the compressible growth rate is enhanced by a factor $\sim(1 + 0.25M_b^2)$, while for $M_b \gg 1$ it is suppressed by a factor $\sim\sqrt{2M_b}$. Thus, for sufficiently high Mach numbers, the instability is suppressed, in qualitative similarity to the compressible sheet.

2.3.3 *Short-wavelength limit*

At short wavelengths, $K \gg 1$, the slab solution converges to the sheet solution, but it does so in different ways depending on the Mach number. We summarize the main points below, providing more details in Appendix D. We begin by searching for solutions to equations (28) where $K \to \infty$ and the right-hand side of

[4] In the special case of $M_b = 1$, the fundamental P-mode has a slightly different form, where $\mathrm{Im}(\omega) \propto k^{7/5}$. See Appendix C for details.

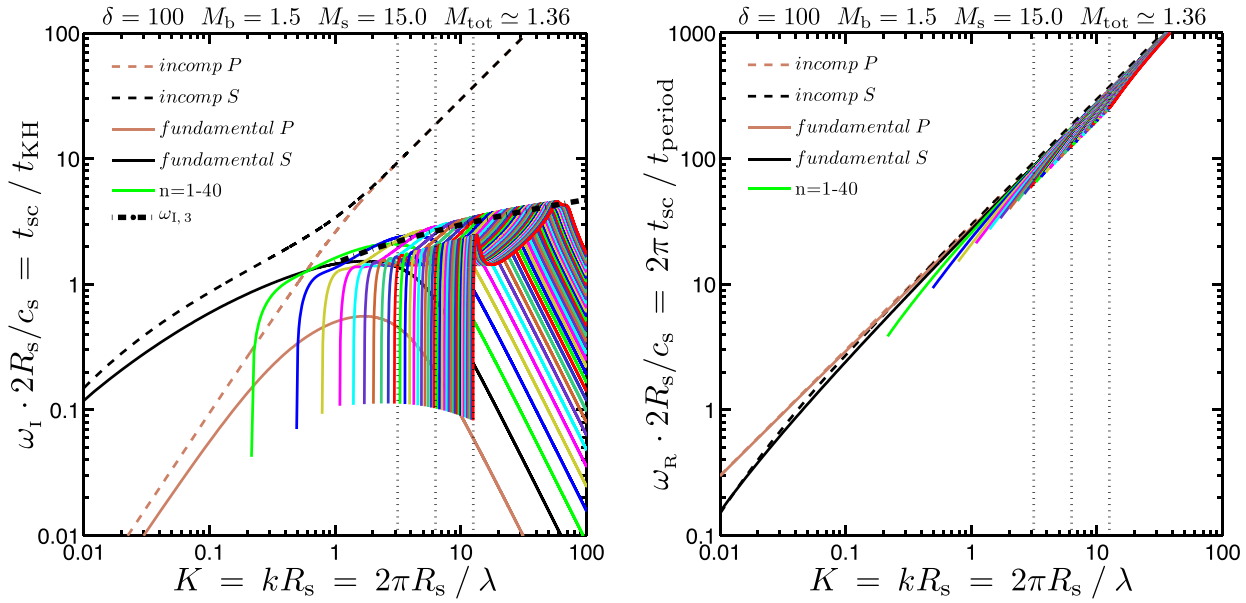

Figure 4. Numerical solution to the slab dispersion relation, equation (27), for $M_b = 1.5$ and $\delta = 100$. For this choice of M_b and δ, the sheet is stable (Fig. 1), while the slab is unstable through body modes. The left-hand panel shows the growth rate, ω_I, normalized by the inverse of the sound-crossing time in the slab, $t_{sc}^{-1} = c_s/(2R_s)$, i.e. the ratio of the sound-crossing time to the Kelvin–Helmholtz time. The right-hand panel shows the oscillation frequency of the wave, ω_R, normalized by t_{sc}^{-1}. The solid black and beige lines show the fundamental (compressible) S- and P-modes, respectively, while the dashed lines show the corresponding solutions for the incompressible slab (equation 29). The coloured lines show the $n = 1$–40 modes ($n = 1$ in green, $n = 2$ in blue, and so on, with even/odd n representing S/P-modes, respectively). At long wavelengths, the two fundamental modes are similar to their incompressible counterparts. However, at $K \gg 1$, the growth rates for the fundamental modes decay while the incompressible modes diverge as $\omega_I \propto k$. Modes with $n \geq 1$ are excited at finite wavenumbers that scale linearly with n, reach a maximum growth rate at resonance and then decay at large K. The vertical dotted lines mark, from left to right, wavelengths of $\lambda = 2R_s$, R_s and $0.5R_s$, where the dominant modes are $n = 2$, 4 and 9, respectively. The ridge line connecting the maximal growth rates of each mode diverges logarithmically, and is well fitted by $\omega_{I,3}$ from equation (36), shown by the thick dash–dotted line. As each mode stabilizes, its phase velocity converges to $\omega_R/k = v - c_s$ (right-hand panel).

equation (28a) is real, since K is real by definition in the temporal stability analysis we are performing.

At low Mach numbers, $M_b \ll 1$, when the sheet is unstable, we have $\mathrm{Im}(q_s) \ll \mathrm{Re}(q_s)$, and the solution is given by $Z = 1$, which is the dispersion relation for the sheet (equation 18). These are *surface modes*, decaying exponentially with depth in the slab. It is unsurprising that such modes resemble the sheet, since in the limit $\lambda \ll R_s$ we expect the perturbations not to be affected by the slab geometry.

At high Mach numbers, $M_b > M_{crit}$, when the sheet is stable, we have $\mathrm{Im}(q_s) > \mathrm{Re}(q_s)$, and the asymptotic solution is given by $1 - \delta M_b^2(1-\varpi)^2 = 0$. This leads to $\varpi = 1 - M_s^{-1} = \varpi_\infty$, which is the high Mach number (stable) limit of the growing mode in the sheet (equation 21). Physically, modes with $\mathrm{Im}(q_s) \gg \mathrm{Re}(q_s)$ are *body modes*, which traverse the width of the slab without decaying, and bring the two interfaces into causal contact. As $\varpi \to \varpi_\infty$, Z goes to zero (equation 18), so equations (28) can be expanded to derive an expression for the asymptotic transverse wavenumber within the slab

$$q_s R_s = \left[1 - \delta M_b^2(\varpi - 1)^2\right]^{1/2} K \simeq \mathrm{i}\frac{(n+2)\pi}{2}. \quad (31)$$

Note that there is an extra 2π here compared to equations (28), because as K is increased from 0 to ∞, $(1+Z)/(1-Z)$ completes a full revolution about the origin in the complex plane, while its argument is defined in the range $(-\pi, \pi$; Appendix F). These represent standing waves within the slab, with wavelengths $\lambda_\perp = 4R_s/(n+2)$. So the nth mode has $n+1$ nodes across the slab width of $2R_s$, which can be seen qualitatively in Fig. 5. The slab acts as a waveguide for these modes, each of which has phase velocity $\omega/k = v - c_s$. This is a qualitatively new phenomenon compared to the sheet. In Section 2.3.4, we show that each of these modes is unstable at finite wavelengths, and characterize the instability. Therefore, while each individual mode (each individual n) converges to the vortex sheet solution at short wavelengths for all Mach numbers, the appearance of higher order unstable modes at shorter and shorter wavelengths renders the slab unstable at all Mach numbers, unlike the sheet which is stable at high M_b.

2.3.4 *Unstable body modes*

At long wavelengths, solutions to the dispersion relation (equations 28) exist only for $n = -1, 0$. In the incompressible limit, $M_b \ll 1$, these are the only two solutions at any wavelength. However, at high Mach numbers, there are an infinite number of *body mode* solutions at short wavelengths. The questions we need to address are when do these modes appear, whether they are unstable and what their growth rate is. These are answered in detail in Appendices E to H, and we summarize the main results below.

From equations (18) and (28), we see that when $\varpi = 0$ the wavenumber of the nth mode is $K_{n,0} = n\pi/(2\sqrt{M_s^2 - 1})$. Since K must be real, such solutions are only possible for $n \geq 1$ if $M_s > 1$. This was incorrectly identified by previous authors (e.g. Payne & Cohn 1985; Hardee & Norman 1988) as the condition for unstable body modes. However, for every $n \geq 1$, the solution $(\varpi, K) = (0, K_{n,0})$ is *stable*, meaning that solutions to the dispersion relation with $K \gtrsim K_{n,0}$ have real ϖ. A necessary and sufficient

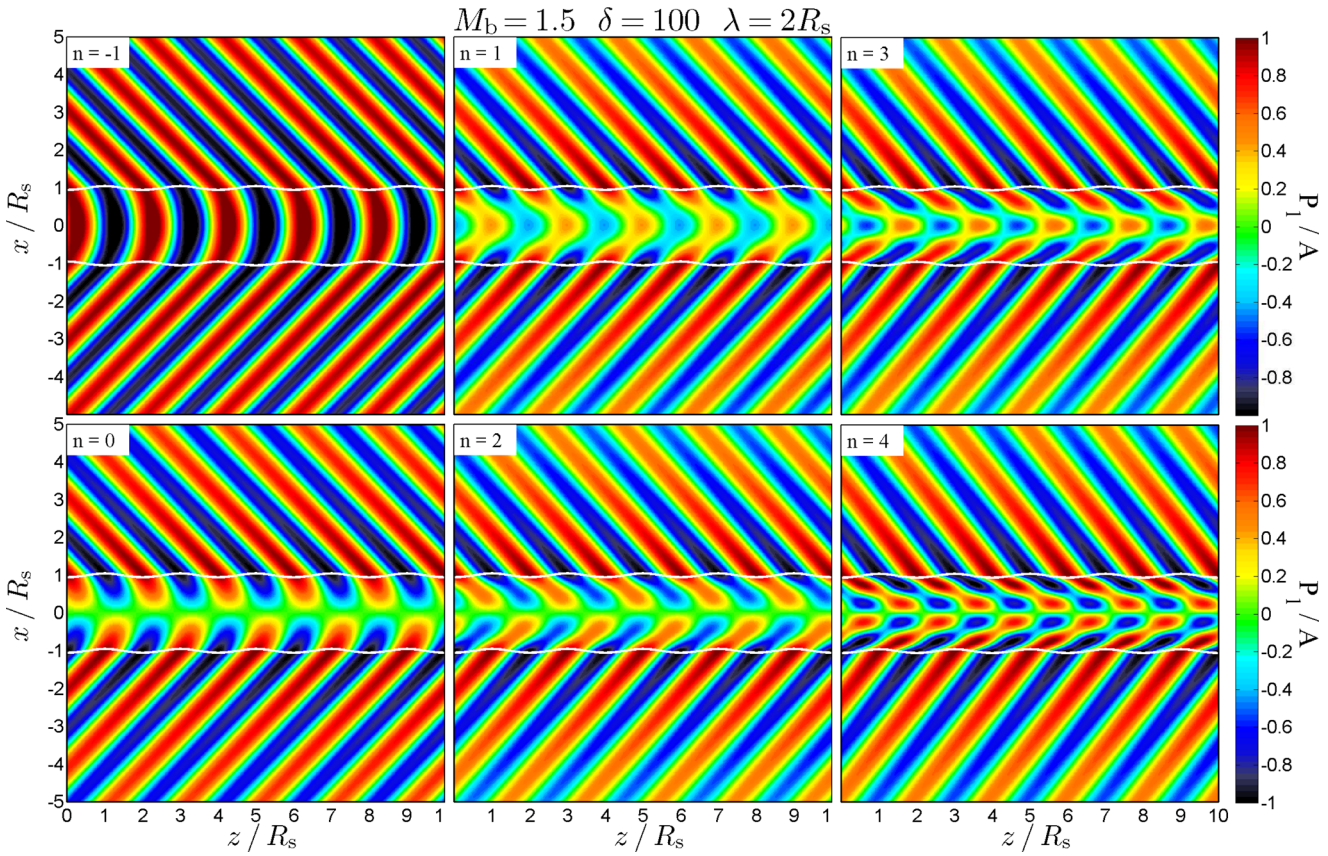

Figure 5. Pressure perturbation in a slab with $M_b = 1.5$ and $\delta = 100$ normalized by its maximal value at the interfaces, A (equation 23), for the first six unstable modes. The longitudinal wavelength of the perturbation (along z) is equal to the slab diameter, $\lambda = 2R_s$, and the amplitude of fluid displacement at the interfaces is $h = 0.025\lambda$, which is shown by the white curves. The top row shows the first three P-modes: $n = -1$ (the fundamental mode, left), $n = 1$ (centre) and $n = 3$ (right). The bottom row shows the first three S-modes: $n = 0$ (the fundamental mode, left), $n = 2$ (centre) and $n = 4$ (right). All unstable modes for this case are *body modes*, which penetrate to large depths in both the slab and the background. The number of transverse nodes within the slab (along x) is $(n + 1)$, creating a more complex standing wave pattern as n increases.

condition for body modes to be unstable is not $M_s > 1$, but rather (Appendix E)

$$M_{tot} = \frac{V}{c_s + c_b} = \frac{\sqrt{\delta}}{1 + \sqrt{\delta}} M_b > 1. \tag{32}$$

If $M_{tot} < 1$, only the fundamental modes with $n = -1, 0$ are unstable, and these modes are surface modes.[5]

When $M_{tot} > 1$, the smallest unstable wavenumber (corresponding to the longest unstable wavelength, and hereafter referred to as marginal stability) for the nth body mode is well approximated by (Appendix F)

$$K_n \simeq \frac{n\pi}{2\sqrt{\delta(M_b - 1)^2 - 1}}. \tag{33}$$

Defining $\kappa \equiv K - K_n$, the growth rate of the nth body mode near marginal stability scales as (Appendix G)

$$\mathrm{Im}(\varpi_n) \propto \delta^{1/4} M_b^2 n^{-3/2} \kappa^{1/2}. \tag{34}$$

This growth rate diverges strongly with Mach number, which is in contrast to the fundamental modes. Recall that near marginal stability at $K = 0$, the growth rate of the fundamental S-mode was independent of M_b, while the growth rate of the fundamental P-mode scaled as $M_b^{-1/2}$ (equations 30).

Since the growth rate of each mode goes to zero as $K \to \infty$ (Section 2.3.3), it must reach a maximum at some intermediate K, hereafter the mode *resonance*. The resonant wavenumber is well approximated by (Appendix H)

$$K_{n,\,res} \simeq \frac{n\pi}{2M_{tot}}. \tag{35}$$

At a given wavelength, the effective growth rate of the slab is determined by the mode with the largest growth rate at that wavelength (see Fig. 4). This growth rate, $\omega_I = \mathrm{Im}(\omega)$, can be written as the limit of an infinite sequence of functions (Appendix H)

$$\omega_{I,\,1} = t_{sc}^{-1} \ln\left(4M_{tot} \frac{\sqrt{\delta}}{1 + \sqrt{\delta}} K\right) \tag{36a}$$

$$\omega_{I,\,j} = \omega_{I,\,1} - t_{sc}^{-1} \ln\left(t_{sc}\omega_{I,\,j-1}\right), \tag{36b}$$

where $\omega_I = \lim_{j\to\infty} \omega_{I,\,j}$ and

$$t_{sc} = 2R_s/c_s \tag{37}$$

is the slab sound-crossing time. In practice, the sequence converges by $j = 3$ even for relatively low values of K (Fig. H2). In the asymptotic limit $K \to \infty$, $\omega_I \propto \ln(K)$. Hence, the effective growth rate for KHI in a compressible slab diverges logarithmically with

[5] Note that when $\delta \ll 1$, which was the regime studied by Payne & Cohn (1985) and Hardee & Norman (1988), $M_{tot} \sim M_s$.

wavenumber. In contrast, the growth rate for an incompressible sheet or slab diverges linearly with wavenumber, $\omega_{\rm I} \propto k$, while the compressible sheet becomes stable at high Mach numbers, $\omega_{\rm I} = 0$. The scaling of $\omega_{\rm I} \propto \ln(k)$ for the effective growth rate of the compressible slab is in some sense a compromise between these two extremes, though recall that each individual mode does stabilize as $k \rightarrow \infty$ (Section 2.3.3).

At resonance, $q_{\rm b} \simeq q_{\rm s}$ (Appendix H). This means that the penetration depth of the perturbation, $\Delta_{\rm b,\,s} = 1/{\rm Re}(q_{\rm b,\,s})$, is comparable in both the background and the slab. Furthermore, the propagation angle of the perturbation wave with respect to the normal to slab, given by $\cot(\theta_{\rm b,\,s}) = {\rm Im}(q_{\rm b,\,s})/k$, is the same in both media (see Fig. 5, panels marked $n = 1$ and $n = 2$). At resonance, we have $\sin(\theta_{\rm b,s}) \simeq M_{\rm tot}^{-1}$, commonly referred to as *the Mach angle*.

The physical origin of body modes in a slab can be understood in the following way. When a perturbation is excited, the two interfaces between the slab and the background initially behave as independent sheets, only coming into causal contact once a slab sound-crossing time has elapsed. At high Mach numbers, surface modes are stable and the perturbation does not grow in amplitude, but rather results in acoustic waves propagating between the two interfaces, being reflected off of and transmitted through them. The pressure perturbation within the slab (equation 24) can be written as the sum of an incident and a reflected wave, with wavenumber $q_{\rm s}$, while the pressure perturbation in the background can be thought of as a transmitted wave, with wavenumber $q_{\rm b}$. At certain critical incident angles, there is constructive interference between waves emanating from different points along the slab, assumed to have infinite extent. It can be shown that the acoustic impedances of the two fluids are equal when $q_{\rm b} = q_{\rm s}$, which is roughly the case at the resonance of body modes (Appendix H). The equal impedances cause the reflectance and transmission coefficients of the system to diverge, which causes the perturbation amplitude to grow. For further details, see Payne & Cohn (1985) and Hardee & Norman (1988). These authors estimated the resonant growth rates of body modes (which they call *reflected modes*) by associating these singularities in the reflectance and transmission coefficients with unstable solutions to the dispersion relation, rather than deriving them directly from the dispersion relation as we do.

2.3.5 *Numerical solution*

We here summarize, in Figs 4 and 5, all the features of unstable body modes in the slab derived above. Fig. 4 shows a numerical solution to the slab dispersion relation, equation (27), for $\delta = 100$ and $M_{\rm b} = 1.5$. We show as a function of wavenumber, $K = kR_{\rm s}$, the growth rate of the perturbation, $\omega_{\rm I} = {\rm Im}(\omega) = t_{\rm KH}^{-1}$ (left), and the oscillation frequency of the wave, $\omega_{\rm R} = {\rm Re}(\omega) = 2\pi t_{\rm period}^{-1}$ (right). In both cases, we normalize the frequency by the inverse sound-crossing time in the slab, $t_{\rm sc}^{-1}$. We show the two fundamental modes ($n = -1, 0$) and the modes $n = 1$–40 (odd/even for P/S-modes). We also show the solutions for the incompressible slab for comparison. Note that for this choice of $M_{\rm b}$ and δ, the sheet is stable (Fig. 1), while the slab is unstable due to body modes.

At long wavelengths, $K \ll 1$, only the fundamental modes are unstable, and their behaviour is similar to the corresponding incompressible solutions. Higher order unstable modes are gradually excited at shorter and shorter wavelengths, according to equation (33). Each mode reaches a maximal growth rate at a resonance wavelength (equation 35), and these dominate over the fundamental modes at intermediate and short wavelengths. At short wavelengths, each mode stabilizes as $\varpi \rightarrow \varpi_\infty = 1 - M_{\rm s}^{-1}$, so that $\omega \rightarrow (v - c_{\rm s})k$. However, the ridge line formed by the peak resonant growth rates acts as an effective growth rate for the slab, which is always unstable. The effective growth rate of this ridge line is well fitted by $\omega_{\rm I} \propto t_{\rm sc}^{-1} \ln(K)$ (equation 36).

Fig. 5 shows the spatial structure of the pressure perturbation in the xz plane, P_1, for the first six unstable modes with $\delta = 100$ and $M_{\rm b} = 1.5$. The longitudinal perturbation wavelength is equal to the slab diameter, $\lambda = 2R_{\rm s}$, and the displacement amplitude of the fluid interfaces is $h = 0.025\lambda$ (shown in white). To compute the transverse wavenumbers, $q_{\rm b,\,s}$, we insert the numerical solutions to the dispersion relation (Fig. 4) into equation (12). The top row shows the first three P-modes: $n = -1$ (the fundamental mode), $n = 1$ and $n = 3$ from left to right. The bottom row shows the first three S-modes: $n = 0$ (the fundamental mode), $n = 2$ and $n = 4$ from left to right. Since sheet is stable for these values of $M_{\rm b}$ and δ, surface modes such as shown in Fig. 2 are stable. All unstable modes, including the fundamentals, are *body modes*, whose exponential decay length in the transverse direction is comparable to or larger than the slab width. The nth mode has $n + 1$ nodes across the slab width, creating a more complex standing wave pattern as n increases. For $\lambda = 2R_{\rm s}$, the $n = 1$ and 2 modes are near resonance, so the angle of wave propagation is nearly the same in the slab and the background. For the other modes, the pattern breaks at the slab interfaces.

2.4 The cylindrical stream

We now consider a flow with cylindrical, rather than planar symmetry. Using the standard cylindrical coordinates, (r, φ, z), we assume an equilibrium configuration where the density and flow velocity depend only on r, the flow is in the $\hat{z}$ direction and the pressure is constant: $\rho_0(r)$, $v_0(r)\hat{z}$, P_0. By rewriting the hydrodynamic equations (equations 1 to 3) in cylindrical coordinates, inserting perturbations of the form $f(r)\,\exp[{\rm i}(kz + m\varphi - \omega t)]$, where m is an integer, and linearizing, we obtain analogous expressions to equations (6)– (9) that relate the perturbations in density and velocity to the pressure perturbation. We also obtain a second-order differential equation for the pressure perturbation, analogous to equation (10):

$$P_1'' - \left[\frac{2v'}{v - \omega/k} + \frac{\rho_0'}{\rho_0} - \frac{1}{r}\right] P_1' - k^2 \left[1 - \left(\frac{v - \omega/k}{c}\right)^2 + \left(\frac{m}{kr}\right)^2\right] P_1 = 0, \tag{38}$$

where $f' = \partial f/\partial r$. This is identical to equation (10), except for the geometrical terms $1/r$ and $m/(kr)$.

We consider an infinitely long cylindrical stream of radius $r = R_{\rm s}$, centred on the z-axis, with density and velocity $\rho = \rho_{\rm s}$ and $\boldsymbol{v} = V\hat{z}$. The background, at $r > R_{\rm s}$, has $\rho = \rho_{\rm b}$ and $\boldsymbol{v} = 0$. Equation (38) reduces to two modified Bessel equations, for $r < R_{\rm s}$ and $r > R_{\rm s}$. Using the boundary conditions that the pressure perturbation is finite at $r = 0$ and $r \rightarrow \infty$ and is continuous at $r = R_{\rm s}$, we obtain the solution

$$P_1(r) = \begin{cases} A\,\frac{\mathcal{I}_{\rm m}(q_{\rm s}r)}{\mathcal{I}_{\rm m}(q_{\rm s}R_{\rm s})} & r < R_{\rm s}, \\ A\,\frac{\mathcal{K}_{\rm m}(q_{\rm b}r)}{\mathcal{K}_{\rm m}(q_{\rm b}R_{\rm s})} & r > R_{\rm s}. \end{cases} \tag{39}$$

$\mathcal{I}_{\rm m}$ and $\mathcal{K}_{\rm m}$ are the mth-order modified Bessel functions of the first and second kind, respectively, and A is a constant of integration. By applying the Landau condition at the stream boundary, in analogy

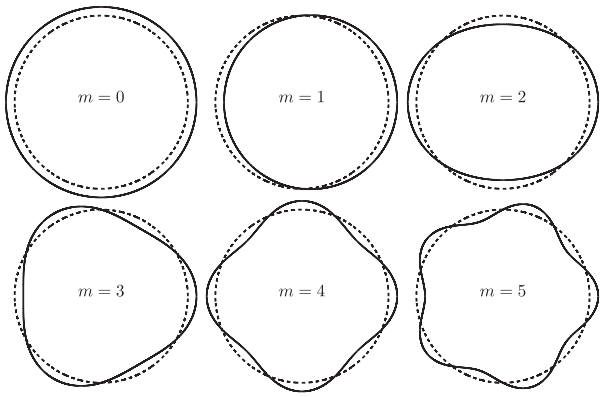

Figure 6. Schematic representation of the first six azimuthal modes for a cylindrical stream, $m = 0$–5. Shown is a slice through the xy plane. The dashed circle in each panel represents the unperturbed cylinder while the solid curve represents the perturbed cylindrical surface. The $m = 0$, 1 modes are analogous to the P,S-modes in the slab case, respectively.

with equation (13), we obtain the dispersion relation

$$Z = -\frac{\mathcal{I}_{\rm m}\left(\sqrt{1-\delta M_{\rm b}^2(\varpi-1)^2}K\right)}{\mathcal{I}'_{\rm m}\left(\sqrt{1-\delta M_{\rm b}^2(\varpi-1)^2}K\right)}\frac{\mathcal{K}'_{\rm m}\left(\sqrt{1-M_{\rm b}^2\varpi^2}K\right)}{\mathcal{K}_{\rm m}\left(\sqrt{1-M_{\rm b}^2\varpi^2}K\right)}. \tag{40}$$

Comparing equations (39) and (40) to the corresponding equations for the slab, equations (23) and (27), we see one qualitative difference between the two configurations. While the slab admitted only two symmetry modes, the symmetric P-modes and the antisymmetric S-modes (Fig. 3), the cylinder admits infinitely many symmetry modes, represented by the index m. Through the Landau condition, which introduces the perturbation to the cylinder surface, we learn that m is the number of azimuthal nodes on this surface. This is shown schematically in Fig. 6, where we show a slice through the $z = 0$ plane for the first six symmetry modes, $m = 0$–5. The $m = 0$ modes are axisymmetric *pinch modes*, analogous to the P-modes in the slab. The $m = 1$ modes are antisymmetric *helical modes*, analogous to S-modes in the slab. Modes with $m > 1$ are *fluting modes* with no direct analogue in the slab, but as we shall see they do not qualitatively change the growth of instabilities at short wavelengths.

2.4.1 Long-wavelength behaviour

At long wavelengths, $K \to 0$, we use the asymptotic form of the modified Bessel functions for $\xi \ll 1$ (Abramowitz & Stegun 1965)

$$\mathcal{I}_{\rm m}(\xi) \simeq \begin{cases} 1 - 0.25\xi^2 & m = 0 \\ (2^m m!)^{-1}\ \xi^m & m \geq 1, \end{cases} \tag{41}$$

$$\mathcal{K}_{\rm m}(\xi) \simeq \begin{cases} 1.27 - \ln(\xi) & m = 0 \\ 2^{m-1}(m-1)!\,\xi^{-m} & m \geq 1. \end{cases} \tag{42}$$

Inserting these into equation (40) results in the leading-order dispersion relations

$$\varpi \simeq \begin{cases} 1 + {\rm i}\frac{1}{\sqrt{2\delta}}K\sqrt{\ln\left(\frac{1}{\sqrt{|M_{\rm b}^2-1|}K}\right)} & m = 0 \\ \frac{\delta}{1+\delta} + {\rm i}\frac{\sqrt{\delta}}{1+\delta} & m \geq 1. \end{cases} \tag{43}$$

These modes are unstable at all wavenumbers and for all values of δ and $M_{\rm b}$. They thus represent the *fundamental modes* for the cylinder. As in the slab, each symmetry mode has one fundamental mode. Modes with $m \geq 1$ all have the same growth rate which is independent of Mach number, similar to the fundamental S-mode in the slab (equation 30a). It is fascinating to note that this is exactly the dispersion relation for the incompressible sheet (equation 15). The fundamental $m = 0$ mode is suppressed at large Mach numbers for a given K, qualitatively similar to the fundamental P-mode in the slab (equation 30b).

2.4.2 Short-wavelength behaviour

At short wavelengths, when $K \gg m + 1$, we use the asymptotic form of the modified Bessel functions for $|\xi| \gg m + 1$ (Abramowitz & Stegun 1965)

$$\mathcal{I}_{\rm m}(\xi) \propto \begin{cases} \xi^{-1/2}\,{\rm e}^{\xi} & {\rm Re}(\xi) > 0 \\ |\xi|^{-1/2}\cos\left(|\xi| - \frac{(2m+1)\pi}{4}\right) & \xi = {\rm i}|\xi| \end{cases} \tag{44}$$

$$\mathcal{K}_{\rm m}(\xi) \propto \xi^{-1/2}\,{\rm e}^{-\xi}. \tag{45}$$

Note that these approximations become valid at shorter wavelengths for larger m. Inserting these into equation (40), we obtain the asymptotic form of the dispersion relation[6]

$$Z \simeq \begin{cases} 1 & {\rm Re}(q_{\rm s}) \gg {\rm Im}(q_{\rm s}) \\ \tanh\left(q_{\rm s}R_{\rm s} - {\rm i}\frac{(2m-1)\pi}{4}\right) & {\rm Re}(q_{\rm s}) \ll {\rm Im}(q_{\rm s}). \end{cases} \tag{46}$$

As for slab and sheet geometries, ${\rm Re}(q_{\rm s}) \gg {\rm Im}(q_{\rm s})$ at low Mach numbers, when surface modes are unstable. In this case, the dispersion relations for the sheet, the slab and the cylinder all converge to $Z = 1$. At higher Mach numbers when surface modes are stable, ${\rm Re}(q_{\rm s}) \ll {\rm Im}(q_{\rm s})$, and the dispersion relation for the cylinder becomes very similar to that of the slab. Except for the extra $-{\rm i}\pi/4$ in the argument of the tanh, equation (46) with $m = 0$ and 1 corresponds exactly to equation (27) for P- and S-modes, respectively. We conclude that for any given m, at short enough wavelengths, $\lambda \ll 2\pi R_{\rm s}/(m+1)$, shorter than any features on the cylinder surface, we are not sensitive to the geometry (planar or cylindrical) and the dispersion relation for the cylinder converges to that of the slab.

Given the similarity of equations (46) and (27) for the short-wavelength behaviour of body modes, we can apply our analysis of the slab (Section 2.3.4 and Appendices E to H) to the cylinder as well. It is straightforward to see that our results for the marginally stable wavenumbers (equation 33), the resonant wavenumbers (equation 35) and the asymptotic transverse wavelength across the stream (equation 31) can all be applied to the cylinder under the transformation $n_{\rm slab} \to 2n_{\rm cyl} + m - 1/2$. As in the slab case, the mode number n represents the number of nodes of the perturbation along the stream width (Fig. 5). Most importantly, the effective growth rate of instabilities in the stream, given by the maximal growth rate at each wavenumber (equations 36), is the same in both the slab and the cylinder.

Fig. 7 shows a numerical solution to the cylindrical dispersion relation, equation (40), for $\delta = 100$ and $M_{\rm b} = 1.5$. We show as a function of wavenumber, $K = kR_{\rm s}$, the growth rate of the perturbation, $\omega_{\rm I} = {\rm Im}(\omega) = t_{\rm KH}^{-1}$ normalized by the inverse sound-crossing

[6] Using $\coth({\rm i}x) = -{\rm i}\cot(x)$ and $\tanh(x) = \coth(x - {\rm i}\pi/2)$.

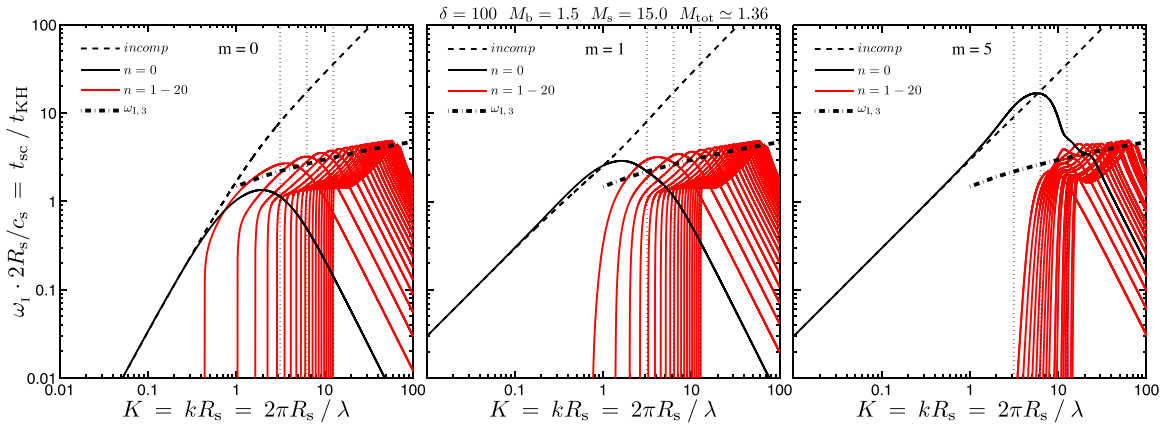

Figure 7. Growth rates for the cylinder. Shown are numerical solutions to the cylinder dispersion relation, equation (40), for $M_b = 1.5$ and $\delta = 100$, the same case shown in Fig. 4 for the slab. The *y*-axis shows the growth rate, ω_I, normalized by the inverse of the sound-crossing time in the stream, $t_{sc}^{-1} = c_s/(2R_s)$, as in the left-hand panel of Fig. 4. The *x*-axis shows the normalized wavenumber $K = kR_s$. We show solutions for $m = 0$ (left), $m = 1$ (centre) and $m = 5$ (right). Dashed black lines show the incompressible solutions. Solid black lines show the fundamental modes, $n = 0$ (one mode for each m). Solid red lines show the $n = 1$–20 modes for each m. Surface modes, where $\omega_I \propto K$, are unstable at wavenumbers $K \lesssim m + 1$ and the corresponding growth rates are very similar to the incompressible case. At shorter wavelengths, body modes dominate the instability, and the effective growth rate due to the ridge line connecting the mode resonances is very similar to the slab case, well fitted by $\omega_{I,3}$ from equation (36) (thick dash–dotted line). Modes with $m > 1$ are expected to be stable for most physical scenarios (see the text), so we expect body modes to dominate the instability for real streams.

time in the stream, t_{sc}^{-1}. This can be directly compared to the corresponding solution for the slab case, shown in the left-hand panel of Fig. 4. The three panels address different azimuthal modes, $m = 0$, 1 and 5 as marked. For each m, we show the fundamental mode, $n = 0$, and the modes $n = 1$–20, together with the corresponding incompressible solution. At long wavelengths, $K < m + 1$, only the fundamental modes are unstable, and their behaviour is similar to the corresponding incompressible solutions. Higher order unstable modes are gradually excited at shorter and shorter wavelengths, and their overall behaviour is similar to the slab case. Most importantly, the effective growth rate for the cylinder at short wavelengths, defined by the ridge line of peak growth rates of each $n \geq 1$ mode, is well fitted by the same formula as for the slab, namely $\omega_I \propto t_{sc}^{-1} \ln(K)$ (equation 36).

2.4.3 *Surface modes versus body modes*

In planar geometry, surface modes become stable when $M_b > M_{crit}$ (equation 22), while body modes in the slab become unstable when $M_{tot} > 1$ (equation 32). However, recall that the Mach number was defined using only the component of the velocity parallel to the perturbation wavevector, $v_k = \boldsymbol{v} \cdot \hat{k}$ (equation 10). On the surface of the cylinder, the wavevector is $\boldsymbol{k} = k\hat{z} + (m/R)\hat{\varphi}$, resulting in $v_k = v[1 + (m/K)^2]^{-1/2}$. Therefore, the effective value of M_b which is relevant for determining whether surface modes are stable is reduced by a factor $[1 + (m/K)^2]^{-1/2}$, which depends both on the azimuthal wavenumber m and on the perturbation wavelength through K. As a result, at a given wavenumber, surface modes will be unstable for azimuthal modes $m > K[(M_b/M_{crit})^2 - 1]^{1/2}$. This means that surface modes are formally *always* unstable for the cylinder, whatever the value of M_b, for large enough m. While this may seem fundamentally different from the slab, it is actually very similar. Recall that we limited our analysis in Sections 2.2 and 2.3 to perturbations where $\boldsymbol{k}||\boldsymbol{v}$, so that $v_k = v$. In principle, perturbations in a slab can assume any angle φ with respect to the flow velocity, and surface modes will be unstable so long as $\cos(\varphi) < M_{crit}/M_b$.

However, surface tension can stabilize modes with $m \geq 2$, where the stream surface is highly perturbed with many small-scale features and the surface-to-volume ratio is high (see Fig. 6). Previous studies have found that the inclusion of magnetic fields parallel to the flow, which act as a form of surface tension, stabilizes surface modes with $m \geq 2$ (e.g. Ferrari, Trussoni & Zaninetti 1981; Birkinshaw 1990). Furthermore, perturbations with $m = 0$–2 are likely the dominant modes in cold streams in galactic haloes, plausibly seeded by gravitational tidal interactions with satellite galaxies located either inside or outside the streams. We will therefore focus hereafter on low-m modes, where body modes dominate the instability for wavelengths $\lambda \lesssim R_s$.

3 SIMULATION RESULTS

In this section, we use numerical simulations to study the growth of perturbations due to KHI in the linear regime. Guided by Section 2, we do this in two stages. First, we study the evolution of *eigenmode* perturbations, whose initial spatial structure obeys the linearized equations of hydrodynamics as derived in Section 2. This corresponds to a pressure perturbation obeying equation (11) for a sheet, equations (23) and (24) for a slab, or equation (38) for a cylinder, together with perturbations in the density and velocity obeying equations (6)–(9) in planar geometry, or the corresponding equations in cylindrical geometry. In the second stage, we study the evolution of arbitrary *non-eigenmode* perturbations.

3.1 Numerical method

We use the Eulerian code RAMSES (Teyssier 2002), with a piecewise-linear reconstruction using the MonCen slope limiter (van Leer 1977) and an HLLC approximate Riemann solver (Toro, Spruce & Speares 1994). Since perturbations with wavelengths $\lambda \lesssim R_s$ in a slab and a cylinder should behave similarly in the linear regime, which is what interests us here, we limit our current analysis to 2D slab simulations. This allows us to achieve higher resolution than would be possible in 3D simulations of cylindrical streams. As highlighted below, the slab simulations also allow us to test our predictions for the sheet.

Table 1. The top five entries correspond to the eigenmode runs (Section 3.2), the bottom three to the non-eigenmode runs (Section 3.3). For each simulation, we list the values of δ, $M_{\rm b}$ and $M_{\rm tot}$; whether it corresponds to a surface (S) or body (B) mode; the mode number, n; the ratio of the perturbation wavelength, λ, to the slab radius, $R_{\rm s}$, the smoothing scale, σ (equation 48), and the smallest cell size, Δ; and the KH time, $t_{\rm KH}$ (equation 47), in units of the box sound-crossing time, $T_{\rm box}$. For eigenmodes, n and $t_{\rm KH}$ correspond to the seeded mode. For the non-eigenmode runs, they correspond to the fastest growing mode for the given δ, $M_{\rm b}$, λ and mode symmetry (they are all symmetric P-modes).

Parameters of the simulations								
δ	$M_{\rm b}$	$M_{\rm tot}$	S/B	n	$\lambda/R_{\rm s}$	λ/σ	λ/Δ	$t_{\rm KH}/T_{\rm box}$
1	1.5	0.75	S	0	2	102	410	0.004
10	1.5	1.13	S	0	2	102	410	0.009
10	1.5	1.13	B	2	2	25	410	0.038
100	1.5	1.36	B	2	2	102	410	0.053
1	5.0	2.50	B	4	2	102	410	0.006
1	1.5	0.75	S	−1	1	102	205	0.002
10	1.5	1.13	S	−1	1	102	205	0.004
1	5.0	2.50	B	5	1	102	205	0.005

The simulation domain is a square of side $L = 1$, representing the xz plane, extending from 0 to 1 in the z direction and from -0.5 to 0.5 in the x direction. The slab is centred at $x = 0$ with a radius of $R_{\rm s} = 1/160$, and extends the full domain in the z direction. We use periodic boundary conditions at $z = 0$ and 1, and outflow boundary conditions at $x = \pm 0.5$ (such that gas crossing the boundary is lost from the simulation domain). The slab and the background are both ideal gases with adiabatic index $\gamma = 5/3$ and initial uniform pressure $P_0 = 1$. The background, at $|x| > R_{\rm s}$, is initialized with density $\rho_{\rm b} = 1$ and velocity $\boldsymbol{v}_{\rm b,\,0} = 0$. The slab, at $|x| < R_{\rm s}$, is initialized with $\rho_{\rm s} = \delta$ and $\boldsymbol{v}_{\rm s,\,0} = M_{\rm b} c_{\rm b} \hat{z}$, where $c_{\rm b}$ is the sound speed in the background, $(5/3)^{1/2}$ in simulation units. We simulate several different combinations of δ and $M_{\rm b}$ (Table 1).

A characteristic time common to all our simulations is the sound-crossing time in the background, $T_{\rm box} = L/c_{\rm b} \sim 0.775$ in our simulation units. The characteristic time for growth of perturbations in the linear regime is the *Kelvin–Helmholtz time*, $t_{\rm KH}$. This is the inverse of the imaginary part of the frequency, $t_{\rm KH} = \omega_{\rm I}^{-1} = (kV\varpi_{\rm I})^{-1}$, and can be expressed as

$$t_{\rm KH} = \left[2K\delta^{1/2} M_{\rm b}\, \varpi_{\rm I}\right]^{-1} t_{\rm sc}, \tag{47}$$

with $t_{\rm sc} = 2R_{\rm s}/c_{\rm s}$ the sound-crossing time in the slab (equation 37). We run each simulation for at least $5t_{\rm KH}$ with 20 outputs per $t_{\rm KH}$. Our use of a thin slab with $R_{\rm s} \ll L$ ensures that $t_{\rm KH} \ll T_{\rm box}$ in all of our simulations (Table 1). The boundary conditions at $x = \pm 0.5$ are thus unimportant as the boundary and the slab are not in causal contact at any point during the simulation.

In the setup described above, the density and velocity are discontinuous at the slab boundaries, $x = \pm R_{\rm s}$. While this is the case we solved analytically in Section 2, such a setup is problematic to simulate as it leads to numerical noise at the grid scale[7] (e.g. Robertson et al. 2010), causing artificial small-scale perturbations. Since shorter wavelength perturbations grow faster, these can quickly dominate over the seeded perturbation. Increasing the resolution decreases the wavelengths of the numerical noise and increases its growth rate, thus making the problem worse. To get around this, we smooth the density and velocity using a ramp function

$$f(x) = f_{\rm b} + 0.25(f_{\rm s} - f_{\rm b}) \times \left[1 + \tanh\left(\frac{R_{\rm s} - x}{\sigma}\right)\right]\left[1 + \tanh\left(\frac{R_{\rm s} + x}{\sigma}\right)\right]. \tag{48}$$

This creates a finite shearing layer between the slab and the background, with a width of $\sim 3\sigma$ for 95 per cent convergence, which suppresses the growth of perturbations with wavelengths comparable to or smaller than the shearing layer (Robertson et al. 2010). In order to effectively suppress the grid noise, we find that we require $\sigma > 2\Delta$, where Δ is the cell size.

While RAMSES has AMR capabilities, we instead use a statically refined grid. The region $|x| < 5R_{\rm s}$ has the highest resolution, with cell size Δ, and the cell size increases by a factor of 2 every $5R_{\rm s}$ in the x direction until a maximal cell size. In all our simulations, $\Delta = 2^{-15} \simeq R_{\rm s}/205$, and the maximal cell size was 2^{-9}.

In order for our analytical solution of a sharp discontinuity to be valid, the eigenmode structure must be well resolved. For surface modes, this means resolving the exponential decay length of the perturbation. Since the perturbation decays more rapidly in the denser fluid (Fig. 2), the eigenmode is resolved if $\sigma \ll 1/{\rm Re}(q_{\rm s})$, which for $\delta \sim$ 10–100 corresponds to $\sigma \ll 0.1$–$0.3\,\lambda$. Thus, properly resolving the eigenmodes while at the same time suppressing artificial perturbations requires $\Delta < 0.5\sigma \ll 0.1\lambda$. In practice, we find that our results are well converged for $\lambda > 30\sigma > 60\Delta$. Body modes are easier to resolve. The smallest length-scale we must resolve is the transverse wavelength within the slab, $2\pi/{\rm Im}(q_{\rm s}) \sim 4R_{\rm s}/(n+2)$ (equation 31). For $\lambda \lesssim R_{\rm s}$, $\delta \sim$ 10–100 and $M_{\rm b} \lesssim 2$, typical of cold streams in haloes (Section 4), the fastest growing mode has $n \lesssim 10$ (equation 35), yielding the requirement $\sigma \ll 0.3\,\lambda$. Table 1 compares Δ, σ and λ for each simulation.

3.2 Eigenmode simulations

Eigenmodes are simultaneous perturbations of all the fluid variables that self-consistently solve the linearized equations of hydrodynamics. To find the true eigenmodes of the problem, we would have to insert the smoothed density and velocity profiles given by equation (48) into equation (10), solve the ODE to find the form of the pressure perturbation, and then insert this into equations (6)–(9) to find the corresponding perturbations in density and velocity. However, there is no analytic solution to equation (10) with the profiles given by equation (48), and this would not offer a direct test of the growth rates derived in Section 2. Instead, we approximate the eigenmodes of the smoothed profile as smoothed versions of the eigenmodes corresponding to the 'step-function' profile. More precisely, we take the pressure perturbation given by equations (23) and (24), and insert this into equations (6)–(9) assuming constant density and velocity within each region (slab and background) to find the corresponding density and velocity perturbations. As these are also discontinuous at $x = \pm R_{\rm s}$, we smooth them using equation (48) as well. This approximation for the eigenmodes, and subsequently the general discussion of a step-function slab, will be judged by how well the simulations match the predicted evolution of eigenmodes, namely that they grow exponentially in amplitude from $t = 0$ while maintaining their spatial structure.

Based on the analysis in Section 2, there are three regimes of instability for a slab, depending on the values of $M_{\rm tot}$ and δ. To see this, it is useful to define

$$M_{\rm tot,\,crit} \equiv M_{\rm crit}\frac{\delta^{1/2}}{1+\delta^{1/2}} = \frac{\left(1+\delta^{1/3}\right)^{3/2}}{1+\delta^{1/2}}, \tag{49}$$

[7] One source of noise comes from trying to capture a sinusoidal shape of the slab boundary using a finite Cartesian grid, which leads to inaccuracies on the grid scale.

where $M_{\rm crit}$ is the critical value of $M_{\rm b}$ above which surface modes become stable (equation 22). $M_{\rm tot,\,crit}$ is the corresponding critical value of $M_{\rm tot}$. It is straightforward to show that $M_{\rm tot,\,crit} > 1$ for any finite δ. The three regimes of instability are thus as follows.

(i) If $M_{\rm tot} < 1$, then *surface modes are unstable*, while *body modes are stable*. The only unstable modes are the two fundamental modes, $n = -1, 0$.

(ii) If $1 < M_{\rm tot} < M_{\rm tot,\,crit}$, then *both surface modes and body modes are unstable*. The fundamental modes correspond to unstable surface modes while modes with $n \geq 1$ correspond to unstable body modes.

(iii) If $M_{\rm tot} > M_{\rm tot,\,crit}$, then *surface modes are stable* while *body modes are unstable*. All modes including the fundamentals correspond to unstable body modes.

To explore the three regimes, we ran a total of five eigenmode simulations. Relevant parameters of these simulations are listed in Table 1. The case $(\delta, M_{\rm b}) = (1, 1.5)$ represents the first regime where only surface modes are unstable. The case $(\delta, M_{\rm b}) = (10, 1.5)$ represents the second regime where both surface and body modes are unstable, and we simulate one of each: the $n = 0$ surface mode and the $n = 2$ body mode. The cases $(\delta, M_{\rm b}) = (100, 1.5)$ and $(\delta, M_{\rm b}) = (1, 5.0)$ represent the third regime where only body modes are unstable, and we simulate the $n = 2$ and 4 modes, respectively.[8] Note that all simulated modes correspond to S-modes with even mode number, n. We normalize all perturbation amplitudes by setting $A = 0.05$ in equations (23) and (24) and set the perturbation wavelength equal to the slab width, $\lambda = 2R_{\rm s}$, yielding $K = \pi$.

The predicted complex frequency corresponding to each simulated mode, ϖ, is found by numerically solving the dispersion relation, equation (27). For surface modes, these are nearly identical to the corresponding values in the sheet given by equation (20). The Kelvin–Helmholtz time, $t_{\rm KH}$, is then calculated using equation (47), and listed in Table 1. Each simulation was run until time $t = 5t_{\rm KH}$, which corresponds to a different time for each mode. Table 1 also shows the ratio of the wavelength to the smoothing scale, σ, from equation (48). In most cases, we use relatively narrow smoothing, $\sigma = \lambda/102$, in order not to deviate too far from the step-function slab. However, for the $\delta = 10$ body mode, we require a larger smoothing scale, $\sigma = \lambda/25$, to suppress artificial surface modes which have much faster growth rates than the body mode. This is less of an issue in the third regime where surface modes are intrinsically stable.

In each snapshot, we estimate the perturbation amplitude by calculating the average of $|P_1| = |P - P_0| = |P - 1|$ in the high-resolution region, $|x| < 5R_{\rm s}$. We experimented with varying the region within which we average the perturbation between $|x| < R_{\rm s}$ and $|x| < 5R_{\rm s}$, calculating the root-mean-squared value of P_1 rather than the averaged absolute value, and using the transverse velocity or the displacement of the slab interface[9] rather than the pressure to estimate the perturbation amplitude. These variations change our growth rates by less than ∼10 per cent.

Fig. 8 shows the perturbation amplitude as a function of time, normalized by the respective value of $t_{\rm KH}$ from Table 1, for the five eigenmode simulations. The analytical prediction is that eigenmode perturbations grow exponentially from time $t = 0$, their amplitude

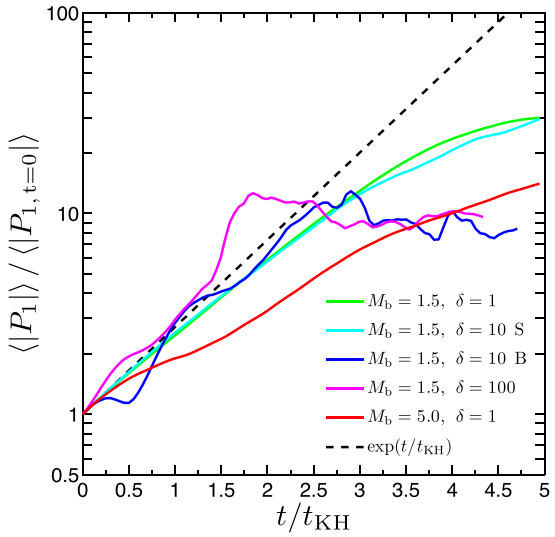

Figure 8. Growth rate of eigenmode perturbations in the numerical simulations, represented by the five solid curves. The x-axis shows time normalized by the respective KH time for each mode according to Table 1. Each simulation was run for $5t_{\rm KH}$, corresponding to a longer time for higher δ and for body modes compared to surface modes. The y-axis shows the pressure perturbation amplitude normalized by its value at $t = 0$. The dashed line marks the expected exponential growth. All simulations match the analytically predicted growth rate to within ∼20 per cent for a period of between ∼1.5 and $3t_{\rm KH}$, after which the growth rate saturates due to non-linear effects.

scaling as $\exp(t/t_{\rm KH})$, which is shown by the dashed line. All simulated modes match the predicted growth rate to within ∼20 per cent for a period of between 1.5 and $3t_{\rm KH}$. The largest deviation occurs for the case $(\delta, M_{\rm b}) = (1, 5.0)$, where the measured growth rate is ∼20 per cent below the predicted value. This is presumably caused by numerical diffusion, more severe for higher Mach number flows (Robertson et al. 2010), as this mode has the highest value of $M_{\rm tot}$ by nearly a factor of 2. For the $(\delta, M_{\rm b}) = (100, 1.5)$ mode, the growth rate increases sharply at $t \sim 1.5t_{\rm KH}$. This is due to mixing of the slab and the background which causes the effective density contrast and Mach number to decrease slightly, rendering the configuration unstable to artificial (numerical) surface modes, as the initial configuration was already very close to the critical Mach number. In the other three simulations, the growth rate is well behaved until $t \sim 3t_{\rm KH}$, at which point non-linear effects cause the amplitude to saturate. A detailed study of the quasi-linear and non-linear phases of the instability, including this saturation, will be the subject of a forthcoming paper (Padnos et al., in preparation).

We have rerun all simulations with twice higher and twice lower resolution while keeping σ/λ fixed, and found no noticeable effect on the results. We also reran the simulations with the same resolution while varying σ/Δ between 1 and 16. Larger values of σ result in slower growth rates compared to the predicted values, especially for surface modes where eigenmodes are harder to resolve (Section 3.1). Smaller values of σ bring the simulated growth rates into better agreement with the predictions at early times, but lead to artificial noise dominating the perturbation amplitude and hence the growth rate before the non-linear saturation of the initial seeded mode.

3.3 Non-eigenmode simulations

We now study the evolution of general perturbations, which are not eigenmodes of the problem. We initialize pressure perturbations

[8] The first of these two cases has $M_{\rm b}$ very close to $M_{\rm crit}$ (see Fig. 1) while the second is deep within the third regime.

[9] This was calculated by using a passive scalar, called 'colour', to differentiate the slab material from the background.

which are harmonic along the slab axis and decaying perpendicular to it:

$$P_1 = A\cos(kz) \times \left[\exp\left(-\frac{(x-R_s)^2}{2\Sigma^2}\right) + \exp\left(-\frac{(x+R_s)^2}{2\Sigma^2}\right)\right], \quad (50)$$

with $A = 0.05$ and $\Sigma = 5\sigma$. The precise value of Σ, the width of the perturbation, is not important as long as it is larger than σ, the width of the smoothing layer. We also tried initializing perturbations in the transverse velocity component, and found no qualitative difference in our results. We prefer to focus here on the pressure perturbations, because all simulations, eigenmode and non-eigenmode, have initially uniform pressure in the entire domain, $P_0 = 1$, whereas the slab velocity and sound speed vary between different simulations.

According to the analysis in Section 2, growing modes are eigenmodes. However, eigenmodes *do not* span the full range of perturbations, and an arbitrary initial perturbation cannot be decomposed into a linear combination of eigenmodes. Each eigenmode contains perturbations in all fluid variables whose amplitudes are linearly related to one another, while different eigenmodes have different transverse wavelengths. Thus, no linear combination of eigenmodes can result in a perturbation in only one fluid variable (such as the pressure) while leaving the others unperturbed. Before an arbitrary initial perturbation in one of the fluid variables can begin to grow, corresponding perturbations in the other variables will develop. The resulting set of perturbations can be decomposed into a linear combination of eigenmodes, both growing and decaying modes, and a residual perturbation. The residual propagates as a sound wave away from the slab boundary, the decaying eigenmodes decay away and eventually the growing eigenmodes dominate. The minimal time-scale over which the fluid can 'arrange' itself into eigenmodes is the wavelength sound-crossing time within the hot medium, $t_\lambda = \lambda/c_b$. At $t > t_\lambda$, after eigenmodes have developed, their amplitudes will begin to grow according to their corresponding growth rates until the fastest growing mode will eventually dominate the instability.

An additional relevant time-scale is the slab sound-crossing time, t_{sc}. At $t < t_{sc}$, the slab is not coherent, and information regarding a perturbation on one edge will not have reached the opposite edge. In our analysis of the dispersion relation for the slab (and the cylinder), we implicitly assumed both boundaries to be in causal contact, so these solutions can only be applied at $t > t_{sc}$. At earlier times, each boundary must behave as an independent sheet. In the regime where surface modes are unstable, the slab and sheet are practically identical anyway, and perturbations begin to grow at $t \gtrsim t_\lambda$. Body modes, on the other hand, can only begin to grow once the slab is coherent, at $t \gtrsim t_{sc} > t_\lambda$. These are triggered by sound waves reverberating between the slab boundaries, which is why they have been referred to as *reflected modes* in the literature.

We simulated several configurations, with $(\delta, M_b) = (1, 1.5), (10, 1.5), (1, 5.0)$, similar to our eigenmode runs. Each configuration was run once with a perturbation wavelength $\lambda = 2\pi/k = 2R_s$ (as in the eigenmode runs), and once with $\lambda = R_s$. We focus mainly on the runs with $\lambda = R_s$, summarized in Table 1. There we list the mode number and t_{KH} of the fastest growing mode into which the perturbation can decay given M_b, δ and λ/R_s (surface modes for the first two and a body mode for the third). Since the pressure perturbation we are initiating (equation 50) is symmetric, it can only decay into P-modes.

Fig. 9 shows the perturbation amplitude as a function of time, similar to Fig. 8. The time has been normalized by the t_{KH} corresponding to the fastest growing mode (Table 1). As in Fig. 8, we estimate the perturbation amplitude by the average of $|P_1|$, though we calculate the average in a smaller region, $|x| < 2R_s$, since the initial perturbations were localized on the slab boundaries. However, our results are not strongly dependent on the size of this region, or on whether we use pressure or transverse velocity to estimate the amplitude. For each configuration, we have marked the corresponding t_λ with squares and t_{sc} with stars. As expected, the two surface modes begin to grow in amplitude at $t \sim t_\lambda$ while the body mode does not grow until $t \sim t_{sc}$. During the growth phase, the growth rates match the predicted growth rate of the fastest growing mode to within ~20 per cent, similar to the eigenmode runs.

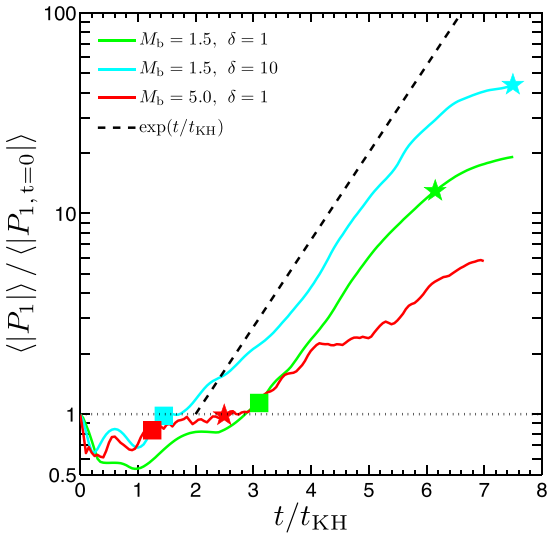

Figure 9. Growth rate of non-eigenmode perturbations in the simulations with wavelengths $\lambda = R_s$, represented by the three solid curves. The x-axis shows time normalized by the KH time of the predicted fastest growing mode given M_b, δ and K, according to Table 1. For the two cases shown with $M_b = 1.5$ (green and cyan curves), the fastest growing mode is a surface mode, while for the case with $M_b = 5$ (red line) it is a body mode. The y-axis shows the perturbation amplitude normalized by its value at $t = 0$, marked by the dotted line. The slope of the dashed line marks the expected exponential growth (the zero-point has been shifted for clarity). Squares mark the wavelength sound-crossing time within the background, $t_\lambda = \lambda/c_b$, after which eigenmodes develop and unstable surface modes begin to grow exponentially. Stars mark the slab sound-crossing time, $t_{sc} = 2R_s/c_s$, after which the two sides of the slab come into causal contact and unstable body modes begin to grow exponentially.

Fig. 10 shows the pressure perturbation for the $(\delta, M_b, \lambda) = (1, 5.0, 2R_s)$ simulation at $t = 0$ and at $t \sim 1.6t_{sc}$, shortly after the perturbation begins to grow. For comparison, we show the analytic form of the corresponding fastest growing P-mode, $n = 5$, normalized to the same amplitude. The fastest growing mode can be found from equation (35) with $K = kR_s = \pi$ and $M_{tot} = 2.5$. The resemblance of the simulation result and the analytic prediction is striking, illustrating that the initial perturbation has evolved into eigenmodes and the fastest growing mode, $n = 5$, dominates.

We also simulated the case $(\delta, M_b) = (100, 1.5)$. Despite surface modes being formally stable for this configuration (Fig. 1), it lies very close to the M_{crit} boundary and small numerical errors seed artificial surface modes. Due to the high density contrast, $t_{sc} \gg t_\lambda$ and these artificial modes dominate the instability before the body mode has a chance to grow.

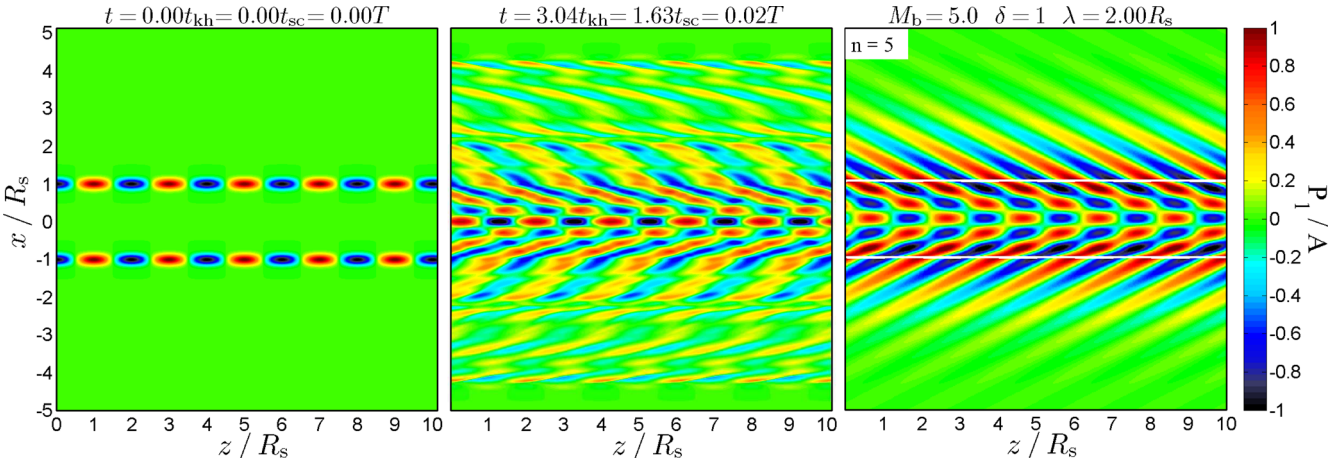

Figure 10. Transition of a general initial perturbation into the fastest growing eigenmode. The left-hand and centre panels are taken from a simulation of a slab with $M_b = 5.0$, $\delta = 1$ and $\lambda = 2R_s$, showing the pressure perturbation, P_1, at time $t = 0$ (left) and $t \sim 1.63t_{sc}$ (centre), after the slab has become coherent. In both panels, we list the time in units of the Kelvin–Helmholtz time of the fastest growing mode, t_{KH}, the slab sound-crossing time, t_{sc}, and the box sound-crossing time, T_{box}. The colour scale has been normalized by A, the maximal value of the perturbation on the slab interface at $t = 0$. The right-hand panel shows the analytic form of the fastest growing mode, the $n = 5$ P-mode, with the amplitude normalized to unity at the slab interface. The resemblance of the simulated perturbation to the analytic mode is striking.

4 LINEAR STABILITY OF COLD FLOWS IN HOT HALOES

In this section, we evaluate the potential importance of KHI in the evolution of cold streams that feed massive galaxies at high redshift. This depends on the ratio of the total time a perturbation can grow before the stream joins the central galaxy, t_{growth}, to the Kelvin–Helmholtz time, t_{KH}. In the linear regime, the amplitude of perturbations grows as $\exp(t/t_{KH})$, so the number of e-foldings in the perturbation growth is

$$N_{\text{e folding}} \equiv t_{growth}/t_{KH}. \tag{51}$$

If $N_{\text{e folding}} = 1, 3$ or 10, a small perturbation will grow to roughly $2.7, 20$ or 2.2×10^4 times its initial amplitude. However, as we saw in Section 3, the exponential growth does not continue indefinitely. Once the perturbation becomes quasi-linear, the amplitude saturates before continuing to grow linearly with time in a self-similar way (Padnos et al., in preparation). For our purposes here, we loosely refer to the cases where $N_{\text{e folding}} \gtrsim 3$ as being quasi-linear and to the cases where $N_{\text{e folding}} \gtrsim 10$ as being non-linear. However, without knowledge of the initial perturbation amplitudes, these thresholds are somewhat arbitrary. All we can say is that if the perturbation begins small, significant growth in the linear regime is a necessary condition for significant growth overall.

We begin by evaluating t_{growth}. For haloes of $M_v \sim 10^{12}\,M_\odot$ at $z \sim 2$, the virial shock radius is roughly the halo virial radius, R_v (e.g. Dekel & Birnboim 2006; Dekel et al. 2009), though we note that in more massive clusters the shocked region can extend to several times R_v (Zinger et al., in preparation). Cosmological simulations indicate that the stream velocity is roughly constant during infall (Dekel et al. 2009; Goerdt et al. 2010; Goerdt & Ceverino 2015), comparable to the halo virial velocity,

$$V \simeq V_v = \sqrt{\frac{GM_v}{R_v}}. \tag{52}$$

The travel time of the stream through the shock-heated medium is thus roughly the virial crossing time

$$t_{infall} \simeq t_v = R_v/V_v. \tag{53}$$

In the Einstein de-Sitter (EdS) regime, valid at $z \gtrsim 1$, this is a constant fraction of the cosmological time, $t_v \simeq 0.14t_{Hubble}$ (e.g. Dekel et al. 2013).

As we saw in Section 3, unstable surface modes begin to grow after the initial perturbation has decayed into eigenmodes, roughly at time $t_\lambda = \lambda/c_b$. We assume $\lambda \lesssim R_s \ll R_v$ and $c_b \sim v_v$ (see below), so $t_\lambda \ll t_v$ and we can assume that surface modes begin to grow instantaneously, $t_{growth} \sim t_v$. On the other hand, unstable body modes can only grow after the stream becomes coherent, at time t_{sc}. Since c_s can be much slower than $c_b \sim v_v$ for a dense stream, t_{sc} can be a significant fraction of t_v, and $t_{growth} \sim t_v - t_{sc}$. The relation between t_{growth} and t_v thus depends on whether surface modes or body modes dominate the instability.

Combining our estimate of t_{growth} for surface/body modes with equation (47) for t_{KH}, we obtain for the number of e-folding times

$$N_{\text{e folding}} = 2K\delta^{1/2}M_b \times \max\left[\varpi_{\text{I, sheet}}\frac{t_v}{t_{sc}},\ \varpi_{\text{I, body}}\left(\frac{t_v}{t_{sc}} - 1\right)\right]. \tag{54}$$

This depends on four parameters: M_b, δ, t_v/t_{sc} and $K = kR_s$. We estimate each of these in turn below.

To estimate M_b for typical cold streams, we make the simplifying assumption that the halo CGM is isothermal. The sound speed in the halo is thus approximately

$$c_b = \sqrt{\frac{\gamma K_B T_v}{\mu m_p}}, \tag{55}$$

where K_B is the Boltzmann constant, T_v is the virial temperature, μm_p is the mean particle mass and $\gamma = 5/3$ is the adiabatic index of the gas. The temperature can be found from virial equilibrium

$$\frac{3}{2}K_B T_v \simeq \frac{1}{2}\frac{GM_v\mu m_p}{R_v} = \frac{1}{2}\mu m_p V_v^2. \tag{56}$$

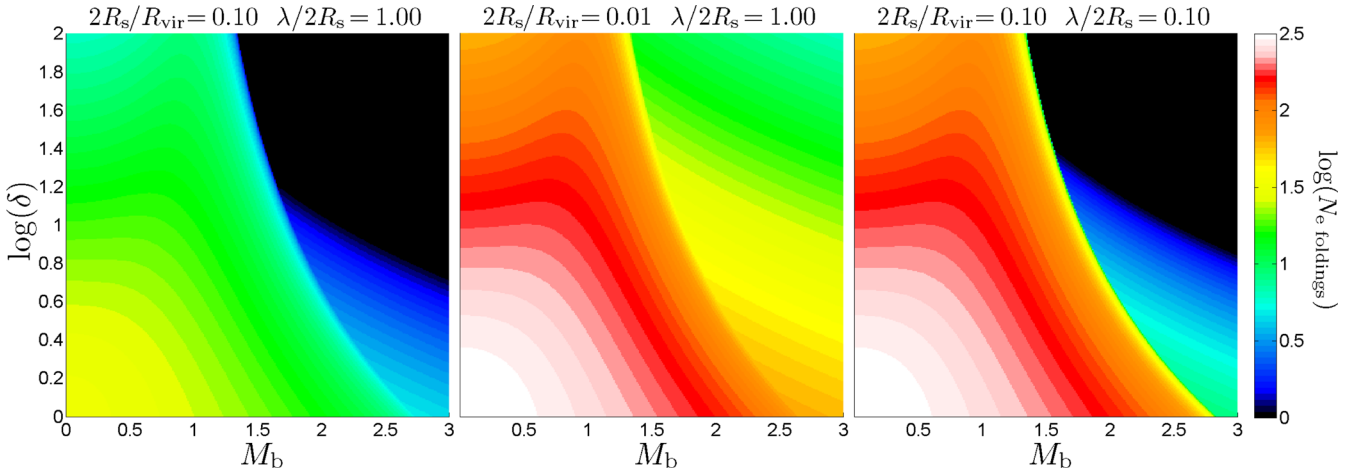

Figure 11. Linear growth of KHI in a virial crossing time, as the stream penetrates from the dark-matter halo virial radius to the central galaxy. Shown in colour is the number of e-foldings of growth in the perturbation amplitude, in the linear regime, as a function of the stream parameters, δ and M_b. The different panels are for different ratios of stream radius to virial radius and perturbation wavelength to stream radius, as listed at the top of each panel. When the sheet is unstable, at $M_b < M_{crit}$ (equation 22), we used the growth rate for surface modes in the sheet (Fig. 1) and allowed the perturbations to grow for a full virial crossing time, $t_v = R_v/v_v$. When the sheet is stable, at $M_b > M_{crit}$, we used the effective resonant growth rate in the slab/cylinder (equations 36 and Fig. 4). In this regime, perturbations begin to grow only after a stream sound-crossing time has elapsed, so they only grow for a time $(t_v - t_{sc})$. The figure shows that realistic values for the stream parameters, $M_b \sim 0.75$–2.25 and $\delta \sim 10$–100, put them near the phase transition between rapid growth of surface modes and slow growth of body modes. While certain regions of parameter space are stable to linear KHI, with $\lesssim$3 e-foldings of growth, a wide range of allowed parameters do result in quasi-linear or non-linear perturbations, with $N_{e\ foldings} \gtrsim 3$ and 10, respectively.

Inserting equation (56) into equation (55) gives for the Mach number of the stream relative to the background $M_b \simeq v_v/c_b \simeq 1.34$. In practice, we assume values in the range $M_b \sim 0.75$–2.25.

To estimate δ, we again make the simplifying assumption that both the halo CGM and the stream are isothermal. The temperature in the halo is $T = T_v$ (equation 56), which for a $\sim 10^{12}\,M_\odot$ halo is a few times 10^6 K. However, due to efficient cooling in the high-density streams, they do not support a stable shock at the virial radius (Dekel & Birnboim 2006), and their temperature is set by the cooling curve for low-metallicity gas, at a few times 10^4 K. Assuming pressure equilibrium between the streams and the hot CGM at any given halo-centric radius, this leads to a density contrast of $\delta \sim 10$–100, consistent with cosmological simulations (e.g. Ocvirk et al. 2008; Dekel et al. 2009; Goerdt et al. 2010).

The ratio t_v/t_{sc} can be related to the ratio of the stream width to the virial radius,

$$t_{sc}/t_v = M_b\, 2R_s/R_v. \tag{57}$$

A narrower stream has a shorter sound-crossing time, leading to more rapid growth of body modes. Based on cosmological simulations, the cold streams we are discussing have characteristic widths of roughly $2R_s/R_v \sim 0.01$–0.1.[10]

The final ingredient is the ratio of the perturbation wavelength to the stream width, $\lambda/(2R_s)$. Since shorter wavelengths grow faster for both surface and body modes, the instability will be dominated by the shortest wavelengths that can grow. In the idealized problem we studied in Section 2, perturbations with arbitrarily small wavelengths can be excited and their growth rate diverges. However, in a realistic stream, there is a finite transition layer at the interface between the stream and the background, similar to the smoothing layer introduced in our simulations (Section 3). Perturbations with wavelengths comparable to or smaller than this layer will be damped. The width of this layer is determined by processes such as thermal conduction and viscosity which are not incorporated in cosmological simulations. This is crudely addressed in Section 5, while a more rigorous study will be the topic of future work. For our purposes, we crudely consider a range of $\lambda/(2R_s) \sim 0.1$–1, corresponding to wavenumbers $K \sim 3$–30. As we have seen, the growth rate scales linearly with wavenumber for surface modes, $\omega_I \propto K$, but only logarithmically for body modes, $\omega_I \propto \ln(K)$.

Fig. 11 shows $N_{e\ folding}$ as a function of M_b and δ for different values of R_s/R_v and λ/R_s. We show a wide stream with $2R_s = 0.1R_v$ and a stream 10 times narrower. We show a long-wavelength perturbation, $\lambda = 2R_s$, and one 10 times smaller. When surface modes dominate the instability, we calculate the growth rates, ϖ_I, from the sheet dispersion relation (equation 20). These are practically identical to the growth rates of surface modes in the slab calculated numerically from equation (27). When body modes dominate the instability, we use the approximation for the fastest growing mode in a slab or a cylinder given by equations (36).

The allowed range for the stream parameters places them near the transition between surface modes and body modes. When surface modes dominate, the stream is highly unstable to KHI in a virial time, and even very small perturbations will become highly non-linear. However, only a very minor change in velocity pushes the stream into the region where body modes dominate and the growth rate is much slower. Wide streams are marginally unstable, with $N_{e\ folding} < 3$. However, narrow streams can be highly unstable even in this regime, with $N_{e\ folding} \lesssim 30$. Furthermore, recall that if $m > 1$ in a cylinder, the effective Mach number for determining whether surface modes are still unstable is $M_b[1 + (m/K)^2]^{-1/2}$ (Section 2.4.3). Thus, for high-m modes, unstable surface modes will occupy a larger region of the parameter space, making Fig. 11 only a lower limit on $N_{e\ folding}$. However, as stated in Section 2.4.3, modes with $m > 1$ are likely to be suppressed in realistic streams,

[10] In realistic haloes, both the stream and the background become denser at smaller radii, making the stream of a conical rather than cylindrical shape. This is discussed further in Section 5.

making our estimates of $N_{\rm e\,folding}$ reasonable. Overall, we estimate that for the relevant range of parameters, $N_{\rm e\,folding} \sim 0.1$–$100$, indicating that KHI can in principle be important for the evolution of cold streams.

5 ADDITIONAL PHYSICS

While the analysis presented here has been thorough and accurate, with interesting new understanding of the body modes in the compressible regime, it has also been very simplistic. We have only studied the linear regime of adiabatic, purely hydrodynamic instabilities. This is an important first step, which allowed us to obtain a definitive result. However, as it stands, further, more detailed analysis is necessary. In a forthcoming paper (Padnos et al., in preparation), we will present a detailed study of the non-linear evolution of idealized KHI, without cooling or gravity. Since we have seen that streams can find themselves in the non-linear regime for a wide range of plausible parameters, this is necessary to complete our study of the effect of KHI in the evolution of cold streams. Additionally, we are planning a series of papers in which we will account for additional physical processes one by one, both analytically as in this work and numerically. Our ultimate goal is to build a comprehensive understanding of the evolution of cold streams, from the bottom up. Below, we outline the additional processes that we intend to address in future work, and their possible effects.

(i) *Cooling.* The importance of cooling in the linear regime of KHI depends on the relation between $t_{\rm KH}$ and the cooling times in the hot and cold media, $t_{\rm h}$ and $t_{\rm c}$, respectively. We will always have $t_{\rm c} < t_{\rm h}$. In the case of cold streams in hot haloes, the cooling time in the hot halo is longer than the virial time, $t_{\rm v} < t_{\rm h}$, which is what allows the presence of a stable virial shock to begin with. Since we are only interested in the cases where $t_{\rm KH} \lesssim t_{\rm v}$, we ignore the case $t_{\rm h} < t_{\rm KH}$.[11] If $t_{\rm KH} < t_{\rm c} < t_{\rm h}$, then cooling should not make any difference in the linear evolution of KHI. However, if $t_{\rm c} < t_{\rm KH} < t_{\rm h}$, then the cold gas returns to an equilibrium temperature fast compared to the hydrodynamic growth time-scale. This is exactly as if the gas were isothermal, and thus all of our analysis stays the same, except that $\gamma = 1$ in the cold medium while $\gamma = 5/3$ in the hot medium. While our analysis implicitly assumed that both media had the same value of γ, this should only affect the ratio of sound speeds and it seems unlikely that this change will dramatically alter our results for the linear evolution. In the non-linear regime, cooling can enhance the instability by introducing thermal instabilities in addition to hydrodynamic ones. Once KHI sets in, regions of the stream will become denser and shocks may develop. The cooling rate in these overdense regions may increase causing them to become even denser and creating a runaway process. However, cooling can also weaken the non-linear evolution of the instability. If the instability is dominated by surface modes, then the non-linear evolution occurs via a shearing layer that forms between the hot and cold media, where the two fluids mix. If the cooling time in the cold stream is shorter than the sound-crossing time, this region will be confined close to the stream boundary and will not consume the stream interior. This effect has been seen in simulations of cold gas clouds surrounded by a hotter confining medium within the interstellar medium (Vietri, Ferrara & Miniati 1997).

(ii) *Thermal conduction.* This can suppress the growth of short-wavelength perturbations, by forming a finite transition region between the stream and the background, similar to the smoothing region in our simulations. Thermal conduction can be treated as a diffusive heat flow with a diffusion coefficient $D(T,\rho) = \kappa(T)/(\rho c_{\rm v})$, where $c_{\rm v}$ is the specific heat capacity and $\kappa(T)$ is the thermal conductivity. Using Spitzer (1956) to evaluate $\kappa(T)$ under the simplifying assumption that both fluids are pure hydrogen, we obtain $D \sim 6\times10^{28}\ {\rm cm^2\ s^{-1}}\ T_6^{5/2} n_4^{-1}$, where T_6 is the gas temperature in units of 10^6 K and n_4 is the gas density in units of $10^{-4}\ {\rm cm^{-3}}$.[12] The characteristic time for diffusion to 'smear out' features with a characteristic length-scale L is $t_{\rm dif} \sim L^2/D$. To estimate the effect this will have on the growth of *surface modes*, we compare $t_{\rm dif}$ over the perturbation wavelength, $L = \lambda$, to the e-folding time for perturbation growth, $t_{\rm KH}$, as surface modes begin to grow immediately (Section 4). For short wavelengths, $\lambda < \lambda_{\rm c} = D/(2\pi M_{\rm b} c_{\rm b} \varpi_{\rm I})$, we have $t_{\rm dif} < t_{\rm KH}$ and we thus expect the instability to be suppressed. For $\delta \sim 100$ and $M_b \sim 1$, we have $\varpi_{\rm I} \sim 0.15$ (Fig. 1). For a virial temperature of $T_{\rm v} \simeq 10^6$ K, we have $c_{\rm b} \sim 1.2\times10^7\ {\rm cm\,s^{-1}}$, and the critical wavelength becomes $\lambda_{\rm c} \sim 1.7\ {\rm kpc}\ T_6^{5/2} n_4^{-1}$. In the cold streams, we estimate $T_6 \sim 0.01$ and $n_4 \sim 100$, yielding $\lambda_{\rm c} \sim 1.7\times10^{-4}$ pc. For the shock-heated halo gas, we have $T_6 \sim n_4 \sim 1$, yielding $\lambda_{\rm c} \sim 1.7$ kpc, comparable to the stream radius. However, in the hot gas, the effective diffusion coefficient is likely to be reduced from the Spitzer (1956) estimate, since the maximum rate of conductive energy transport cannot exceed $\sim v_{\rm e} K_{\rm B} T$, where $v_{\rm e}$ is the electron thermal velocity, i.e. conduction cannot move thermal energy any faster than a population of free-streaming electrons. This can decrease the critical wavelength by at least an order of magnitude. Regarding *body modes*, since these are triggered by sound waves reverberating within the stream, the relevant time-scale is the stream sound-crossing time. Comparing $t_{\rm sc}$ to $t_{\rm dif}$ with $L = 2R_{\rm s}$, $T_6 \sim 0.01$ and $n_4 \sim 100$, we find that heat conduction can suppress the excitement of unstable body modes only if the stream radius is $R_{\rm s} \lesssim 0.1$ pc. While more accurate conclusions await the explicit inclusion of heat conduction in the analysis of KHI, it seems that in cold streams only wavelengths much smaller than the stream width will be suppressed.

(iii) *External gravity.* We refer here to the underlying gravitational potential of the dark-matter halo, which will create a density gradient, and hence a pressure gradient in the background gas halo. As the external pressure increases towards smaller radii, the stream will become narrower towards the halo centre, assuming a conical rather than cylindrical shape. However, we expect our linear analysis as presented in Section 2 to remain valid for perturbations with wavelengths smaller than the length-scale over which the stream radius changes by order unity. If we make the simplifying assumptions that the halo is an isothermal sphere, with $\rho_{\rm b}(r) \propto r^{-2}$ and $T_{\rm b}(r) = {\rm const}$, and that the background and stream are in pressure equilibrium locally at each radius r, then the stream is also isothermal and hence $c_{\rm s}$ is constant. Therefore, the conical shape causes the stream sound-crossing time to decrease towards the halo centre leading to more rapid growth of instabilities, as $t_{\rm KH} \propto t_{\rm sc} \propto R_{\rm s}$. Local pressure equilibrium and the isothermality of the stream imply that the density profile within the stream scales as $\rho_{\rm s}(r) \propto r^{-2}$, which in turn implies that the stream width scales as $R_{\rm s} \propto r$, i.e. a perfect cone with constant opening angle. If the stream velocity is roughly

[11] This could come up in certain physical circumstances, e.g. near an X-ray source that is capable of keeping the hot gas hot.

[12] Similarly, viscosity acts as diffusion in momentum space, but the corresponding diffusion coefficient is ~100 times smaller than for heat conduction (Spitzer 1956).

constant during infall, as indicated by cosmological simulations, this implies that $t_{\rm KH}(r) \propto R_{\rm s}(r) \propto r \propto t_{\rm infall}(r)$. So at every radius, the number of e-foldings a perturbation can grow from its current state before the stream reaches the galaxy is constant. Integrated over the lifetime of the stream, this can lead to significantly more growth than predicted in Section 4. In future work, we will address the dispersion relation of KHI in a conical stream, and perform simulations of streams in an external spherical potential.

(iv) *Self-gravity.* Self-gravity within the stream will have two effects. First, it will result in gradients in density, pressure and perhaps velocity within the stream, as a function of distance from the stream axis. While these gradients will be much weaker than those in the transition zone between the stream and the background, it may still alter the growth rates of perturbations in an appreciable way. Secondly, self-gravity may enhance stream instability by causing overdense regions within the stream to become gravitationally unstable. It is worth noting that a crude estimate of the Jeans scale in the stream is $\lambda_{\rm J} \sim 2\,{\rm kpc}\, c_{10} n_{0.1}^{-1/2}$, where c_{10} is the sound speed in units of $10\,{\rm km\,s^{-1}}$, and $n_{0.1}$ is the gas density in units of $0.1\,{\rm cm^{-3}}$. For $T \sim 10^4$ and $n \sim 0.1$, relevant in the streams near the galaxy, the Jeans length is comparable to the stream width, and could become smaller due to overdensities caused by hydrodynamical and thermal instabilities. We may also witness a fragmentation into sub-filaments, similar to the multi-scale filamentary structure observed in Galactic molecular clouds.

(v) *Magnetic fields.* While the intra-cluster medium (ICM) is known to be mildly magnetized (Churazov et al. 2008), little is known about the magnetization state of gas in galactic haloes. Dubois & Teyssier (2010) argued that initial magnetic fields in the ICM originate from winds outflowing from dwarf galaxies, whose IGM contain magnetic fields well below 1 μG in amplitude. This indicated that the ratio of thermal to magnetic pressure (the plasma β parameter) is $\sim$50–10^3. Furthermore, we expect this to be only an upper limit on the magnetization of the filament gas, which is in general more 'pristine' and has not been affected as much by galactic processes. However, some measurements indicate magnetic fields as high as 0.3 μG in cosmic filaments feeding galaxy clusters (Bagchi et al. 2002). The KH stability of mildly magnetized gas can be altered from its pure hydrodynamic analogue in three ways. The first is the modifications to the equation of state of the gas, though for a sub-dominant component, this effect is expected to be small. The second effect is surface tension that could possibly arise from the shearing of magnetized gas at the boundaries of the instability. The shearing layer is comprised of gas that has been entrained from the filament gas and from the ambient halo, and could be magnetized even when the filament gas is completely unmagnetized, if the halo is not. Through magnetic draping, the magnetic field lines at the shear layer will become aligned with the flow direction, and the amplitude of the magnetic fields there will increase. This process will stabilize the boundary and could strongly affect the results in the linear phases of the instability. We leave for future work a more robust comparison of the growth rate of magnetic fields in the shear layers compared to the growth rate of the instability and their dependence on the initial hydrodynamic perturbation and initial magnetic fields. The third aspect of magnetic fields is its effect on conduction perpendicular to the shearing layer and magnetic draping that is expected there, which could drastically reduce the coefficients of thermal conductivity and viscosity discussed above.

(vi) *Galaxy formation.* Even after accounting for all the effects mentioned above, the analysis will still be idealized. In order to address the stability of realistic cold streams feeding galaxies from the cosmic web, we must account for the presence of additional merging galaxies within the streams, interaction between several streams within the same halo, interaction between streams and feedback induced outflows from the central galaxy, and possible star formation and feedback within the streams themselves. The best way to account for all these effects is with a fully cosmological simulation. In parallel to the methodical work outlined above, we are experimenting with running cosmological zoom-in simulations using RAMSES, with refinement based on gradients in density and velocity, rather than the density-based quasi-Lagrangian strategy typically used (Roca-Fabrega et al., in preparation). This will allow us to resolve the streams better than any existing cosmological simulation. As described in Section 3.1, to properly resolve the instabilities in cold streams, the cell size must be at least $\sim$60 times smaller than the perturbation wavelength. For $\lambda \sim R_{\rm s} \sim 1\,{\rm kpc}$, this corresponds to a resolution of $\lesssim$15 pc within the cold streams, which will be challenging to achieve. Such simulations will also allow us to gauge the effect of initially large instabilities on the streams, such as caused by the collision of a stream with a satellite galaxy in the halo. An idealized study of such a collision suggests that while the stream is initially destroyed, it reforms within $\lesssim$0.3 virial crossing times (Wang et al. 2014), after which our linear analysis is again relevant.

6 SUMMARY AND CONCLUSIONS

We have presented a detailed analysis of linear KHI for fully compressible fluids in three different geometries: a sheet, a slab and a cylindrical stream, confirming our analytical predictions using numerical simulations with RAMSES. We then applied our results to the problem of cold streams that feed massive SFGs at high redshift, showing that KHI can be important in their evolution. For a large region of allowed parameters, the number of e-foldings of growth experienced by a linear perturbation is between 10 and 100. However, the estimated range of parameters overlaps the phase transition between rapidly growing surface modes and more slowly growing body modes. As a result, perturbations may still remain linear by the time the stream reaches the central galaxy, with less than one e-folding of growth in a virial crossing time. The linear analysis of KHI in the adiabatic limit thus indicates that it can be relevant for the evolution of cold streams, but it cannot definitely assess its importance. Our main results can be summarized as follows.

(i) For a sheet, KHI is suppressed at high Mach numbers, $M_{\rm b} > M_{\rm crit} = (1 + \delta^{-1/3})^{3/2}$, with $M_{\rm b} = v/c_{\rm b}$ the fluid velocity normalized by the sound speed in the hot medium, and $\delta = \rho_{\rm s}/\rho_{\rm b}$ the density contrast between the fluids. At lower Mach numbers, the growth rate for instabilities scales linearly with the wavenumber, $\omega_{\rm i} \propto k$, and the perturbations themselves decay exponentially with distance from the interface between the fluids.

(ii) At low Mach numbers, when the sheet is unstable, *surface modes* dominate the instability in a slab, which behaves similarly to a sheet for wavelengths comparable to or shorter than the slab width.

(iii) At high Mach numbers, $M_{\rm tot} = v/(c_{\rm b} + c_{\rm s}) > 1$, the slab remains unstable despite surface modes having stabilized due to the appearance of *body modes* at shorter and shorter wavelengths. These modes are triggered by waves being reflected off the slab boundaries and are qualitatively different than the surface modes present at low Mach numbers. They penetrate the width of the slab, and resemble standing waves propagating through a waveguide. There is an infinite set of these body modes, characterized by a mode number, $n = 1, 2, 3, \ldots$, representing the number of nodes in the

transverse direction. Each mode becomes unstable at a finite wavelength, its growth rate increases towards a maximum at a resonant wavelength and then decays to zero as $\lambda \to 0$. The effective growth rate of instabilities in the slab is given by the sequence of resonant growth rates for each mode. This is inversely proportional to the slab sound-crossing time and scales logarithmically with wavenumber, $\omega_{\rm I} \propto t_{\rm sc}^{-1} \ln(kR_{\rm s})$.

(iv) The only qualitative difference between a slab and a cylinder is that a cylinder has an infinite sequence of symmetry modes, characterized by an azimuthal mode number m, while a slab only has two symmetry modes: symmetric P-modes and antisymmetric S-modes. However, at wavelengths comparable to or shorter than the stream width, the growth rates of instabilities in cylindrical geometry are very similar to those in a slab. The slab is thus a good approximation to the cylinder at short wavelengths.

(v) Simulations of the linear regime of KHI in a slab geometry reproduce the analytic results. When the slab is perturbed with an eigenmode of the problem, so that the initial conditions are self-consistent with the linearized hydrodynamic equations, the growth rate matches the analytic prediction for both surface modes and body modes. When the slab is perturbed by an arbitrary, non-eigenmode perturbation, this must decay into eigenmodes before it can begin to grow. For surface modes, this process lasts for a wavelength sound-crossing time in the hot medium, $t_\lambda = \lambda/c_{\rm h}$. For body modes, we must wait until the stream becomes coherent, after a stream sound-crossing time, $t_{\rm sc} = 2R_{\rm s}/c_{\rm s}$. Once the initial perturbation has decayed into eigenmodes, the fastest growing mode for the given δ, $M_{\rm h}$ and $\lambda/R_{\rm s}$ dominates the instability.

(vi) The allowed range of parameters for cold streams in massive galaxies at high z is near the transition between surface modes and body modes. Thus, even minor variations in the stream parameters within their realistic ranges can have large effects on the growth rate of instabilities. For a realistic range of stream parameters, the number of e-foldings of growth within a virial crossing time can range from roughly 0.1 to 100. This implies that KHI could in principle have an important role in the evolution of cold streams, and a study of the non-linear phases of the instability and the effects of additional physical processes is well motivated.

(vii) When non-linear effects become important, the perturbation amplitude saturates at first, before continuing to grow linearly with time via the mergers of vortices. In an upcoming paper (Padnos et al., in preparation), we will address this process in detail, both analytically and using simulations.

(viii) Rough, order-of-magnitude estimates suggest that heat conduction and magnetic fields should not drastically alter the linear analysis presented here. On the other hand, the gravitational potential of the halo may enhance the instability by causing the stream to become narrower closer to the halo centre, decreasing the sound-crossing time and thus increasing the growth rate of KHI. Cooling is unlikely to drastically affect the linear evolution, but can have significant effects in the non-linear regime. In future work, we will address all these effects one by one in more detail, while in parallel we will study the effects of galaxy formation on cold streams using cosmological simulations with tailored refinement in the streams.

ACKNOWLEDGEMENTS

We thank the referee, J. Xavier Prochaska, for helpful comments that improved the quality of this manuscript. We also thank Romain Teyssier for making RAMSES publicly available. We thank Frederic Bournaud, John Forbes, Sharon Lapiner, Baruch Meerson, Santi Roca-Fabrega, Eva Ntormousi and Almog Yalinewitch for helpful discussions. The simulations were performed on the Astric cluster at HU. This work was supported by ISF grants 24/12, 1059/14 and 1829/12, by BSF grant 2014-273, by the I-CORE Program of the PBC, by NSF grants AST-1010033 and AST-1405962, and by ARC grant DP160100695.

REFERENCES

Abramowitz M., Stegun I., 1965, Handbook of Mathematical Functions. Dover Press, New York
Bagchi J., Ensslin T. A., Miniati F., Stalin C. S., Singh M., Raychaudhury S., Humeshkar N. B., 2002, New Astron., 7, 249
Birkinshaw M., 1984, MNRAS, 208, 887
Birkinshaw M., 1990, Beams and Jets in Astrophysics. Cambridge Univ. Press, Cambridge
Birnboim Y., Dekel A., 2003, MNRAS, 345, 349
Bodo G., Massaglia S., Ferrari A., Trussoni E., 1994, A&A, 283, 655
Bond J. R., Kofman L., Pogosyan D., 1996, Nature, 380, 603
Borisova E. et al., 2016, ApJ, preprint (arXiv:1605.01422)
Bouché N., Murphy M. T., Kacprzak G. G., Péroux C., Contini T., Martin C. L., Dessauges-Zavadsky M., 2013, Science, 341, 50
Bouché N. et al., 2016, ApJ, 820, 121
Cantalupo S., Arrigoni-Battaia F., Prochaska J. X., Hennawi J. F., Madau P., 2014, Nature, 506, 63
Ceverino D., Dekel A., Bournaud F., 2010, MNRAS, 404, 2151
Chandrasekhar S., 1961, Hydrodynamic and Hydromagnetic Stability. Clarendon, Oxford
Churazov E., Forman W., Vikhlinin A., Tremaine S., Gerhard O., Jones C., 2008, MNRAS, 388, 1062
Codis S., Pichon C., Devriendt J., Slyz A., Pogosyan D., Dubois Y., Sousbie T., 2012, MNRAS, 427, 3320
Danovich M., Dekel A., Hahn O., Teyssier R., 2012, MNRAS, 422, 1732
Danovich M., Dekel A., Hahn O., Ceverino D., Primack J., 2015, MNRAS, 449, 2087
Dekel A., Birnboim Y., 2006, MNRAS, 368, 2
Dekel A. et al., 2009, Nature, 457, 451
Dekel A., Zolotov A., Tweed D., Cacciato M., Ceverino D., Primack J. R., 2013, MNRAS, 435, 999
Dijkstra M., Loeb A., 2009, MNRAS, 400, 1109
Dubois Y., Teyssier R., 2010, A&A, 523, A72
Elmegreen D. M., Elmegreen B. G., Ravindranath S., Coe D. A., 2007, ApJ, 658, 763
Faucher-Giguère C.-A., Kereš D., Dijkstra M., Hernquist L., Zaldarriaga M., 2010, ApJ, 725, 633
Faucher-Giguère C.-A., Kereš D., Ma C.-P., 2011, MNRAS, 417, 2982
Ferrari A., Trussoni E., Zaninetti L., 1978, A&A, 64, 43
Ferrari A., Trussoni E., Zaninetti L., 1981, MNRAS, 196, 1051
Förster Schreiber N. M. et al. 2006, ApJ, 645, 1062
Fu H. et al., 2016, ApJ, preprint (arXiv:1607.00016)
Fumagalli M., Prochaska J. X., Kasen D., Dekel A., Ceverino D., Primack J. R., 2011, MNRAS, 418, 1796
Genzel R. et al., 2006, Nature, 442, 786
Genzel R. et al., 2008, ApJ, 687, 59
Goerdt T., Ceverino D., 2015, MNRAS, 450, 3359
Goerdt T., Dekel A., Sternberg A., Ceverino D., Teyssier R., Primack J. R., 2010, MNRAS, 407, 613
Goerdt T., Dekel A., Sternberg A., Gnat O., Ceverino D., 2012, MNRAS, 424, 2292
Hardee P. E., 1987, ApJ, 313, 607
Hardee P. E., Norman M. L., 1988, ApJ, 334, 70
Hopkins A. M., Beacom J. F., 2006, ApJ, 651, 142
Kereš D., Katz N., Weinberg D. H., Davé R., 2005, MNRAS, 363, 2
Kimm T., Devriendt J., Slyz A., Pichon C., Kassin S. A., Dubois Y., 2011, MNRAS, preprint (arXiv:1106.0538)
Landau L. D., 1944, Dokl. Akad. Nauk. SSSR., 44, 139
Madau P., Dickinson M., 2014, ARA&A, 52, 415

Madau P., Pozzetti L., Dickinson M., 1998, ApJ, 498, 106
Matsuda Y., Yamada T., Hayashino T., Yamauchi R., Nakamura Y., 2006, ApJ, 640, L123
Matsuda Y. et al., 2011, MNRAS, 410, L13
Nelson D., Vogelsberger M., Genel S., Sijacki D., Kereš D., Springel V., Hernquist L., 2013, MNRAS, 429, 3353
Norman M. L., Hardee P. E., 1988, ApJ, 334, 80
Ocvirk P., Pichon C., Teyssier R., 2008, MNRAS, 390, 1326
Payne D. G., Cohn H., 1985, ApJ, 291, 655
Perucho M., Hanasz M., Martí J. M., Sol H., 2004, A&A, 427, 415
Pichon C., Pogosyan D., Kimm T., Slyz A., Devriendt J., Dubois Y., 2011, MNRAS, 418, 2493
Press W. H., Schechter P., 1974, ApJ, 187, 425
Prochaska J. X., Lau M. W., Hennawi J. F., 2014, MNRAS, 796, 140
Rees E. L., 1922, Am. Math. Mon., 29, 51
Robertson B. E., Kravtsov A. V., Gnedin N. Y., Abel T., Rudd D. H., 2010, MNRAS, 401, 2463
Spitzer L., 1956, Physics of Fully Ionized Gases. Interscience, New York
Springel V., 2010, MNRAS, 401, 791
Springel V. et al., 2005, Nature, 435, 629
Stark D. P., Swinbank A. M., Ellis R. S., Dye S., Smail I. R., Richard J., 2008, Nature, 455, 775
Steidel C. C., Adelberger K. L., Shapley A. E., Pettini M., Dickinson M., Giavalisco M., 2000, ApJ, 532, 170
Stewart K. R., Kaufmann T., Bullock J. S., Barton E. J., Maller A. H., Diemand J., Wadsley J., 2011, ApJ, 738, 39
Stewart K. R., Brooks A. M., Bullock J. S., Maller A. H., Diemand J., Wadsley J., Moustakas L. A., 2013, ApJ, 769, 74
Teyssier R., 2002, A&A, 385, 337
Toro E. F., Spruce M., Speares W., 1994, Shock Waves, 4, 25
van de Voort F., Schaye J., Booth C. M., Haas M. R., Dalla Vecchia C., 2011, MNRAS, 414, 2458
van de Voort F., Schaye J., Altay G., Theuns T., 2012, MNRAS, 421, 2809
van Leer B., 1977, J. Comput. Phys., 23, 263
Vietri M., Ferrara A., Miniati F., 1997, ApJ, 483, 262
Vogelsberger M., Sijacki D., Kereš D., Springel V., Hernquist L., 2012, MNRAS, 425, 3024
Wang L., Zhu W., Feng L.-L., Macciò A. V., Chang J., Kang X., 2014, MNRAS, 439, L85

APPENDIX A: BRANCH CUTS OF THE SOLUTIONS

Since the generalized wavenumbers $q_{\rm b,\,s}$ (equation 12) are given by the square root of a complex number, we must define a branch cut in the complex plane. As mentioned in Section 2.2, we have chosen to have $\mathrm{Re}(q_{\rm b,\,s}) \geq 0$. This is equivalent to defining arguments of complex numbers between $-\pi$ and π. If the argument of $q^2_{\rm b,s}$ is $2\alpha \in (-\pi, \pi)$, then the argument of $q_{\rm b,\,s}$ is $\alpha \in (-\pi/2, \pi/2)$ and we have $\mathrm{Re}(q_{\rm b,\,s}) > 0$. This ensures that the amplitude of the perturbation decays, rather than grows, away from the interface between the fluids. However, in order to understand how waves generated by the instability propagate away from the interface, we must also determine the sign of $\mathrm{Im}(q_{\rm b,\,s})$. We limit our discussion here to forward travelling growing modes, i.e. modes with $k, \mathrm{Re}(\omega), \mathrm{Im}(\omega) > 0$.

We define $R\exp(\mathrm{i}\theta) \equiv (\omega - kv)/c$. If $\mathrm{Re}(\omega) < kv$, then $\pi/2 < \theta < \pi$ and $q^2 = (k^2 - R^2\cos(2\theta)) - \mathrm{i}(R^2\sin(2\theta))$ has a positive imaginary part. Therefore, if the argument of q is α, we have $0 < 2\alpha < \pi \Rightarrow 0 < \alpha < \pi/2$, which gives $\mathrm{Im}(q) > 0$. On the other hand, if $\mathrm{Re}(\omega) > kv$, similar arguments yield $-\pi/2 < \alpha < 0$, so that $\mathrm{Im}(q) < 0$.

In all cases presented in the text, we assumed that $v_{\rm b} = 0$ and $v_{\rm s} = v$, and found $0 < \mathrm{Re}(\omega) < kV$. This means that $\mathrm{Im}(q_{\rm b}) < 0$ and $\mathrm{Im}(q_{\rm s}) > 0$.

APPENDIX B: SOLVING THE DISPERSION RELATION OF THE COMPRESSIBLE SHEET

In this appendix, we examine the six solutions to equation (20) and explain why only two of them are solutions to the dispersion relation of the compressible sheet (equation 19).

The two solutions to the quadratic part of the equation are $\varpi^2 = \delta(1-\varpi)^2$. Both of these result in $q_{\rm b} = q_{\rm s}$ and in $Z = -1$. Therefore, neither of these are solutions to the dispersion relation, but only come about because equation (19) was squared.

Attempting to find tractable analytic expressions for the four solutions to the quartic part of equation (20) was unsuccessful. However, analytic insight can still be gained by examining its discriminant. Given the general quartic equation

$$f(x) = ax^4 + bx^3 + cx^2 + dx + e, \tag{B1}$$

the discriminant is given by

$$\begin{aligned}\Delta_0 = {} & 256a^3e^3 - 192a^2bde^2 - 128a^2c^2e^2 \\ & + 144a^2cd^2e - 27a^2d^4 + 144ab^2ce^2 - 6ab^2d^2e \\ & - 80abc^2de + 18abcd^3 + 16ac^4e - 4ac^3d^2 \\ & - 27b^4e^2 + 18b^3cde - 4b^3d^3 - 4b^2c^3e + b^2c^2d^2.\end{aligned} \tag{B2}$$

When $\Delta_0 < 0$, the quartic has two real roots and two complex conjugate roots (Rees 1922). For the quartic part of equation (20), we have

$$\begin{aligned}\Delta_0 = {} & 16M_{\rm b}^2\delta^{-4}\cdot[\delta^3M_{\rm b}^6 - 3\delta^2(1+\delta)M_{\rm b}^4 \\ & + 3\delta(\delta^2 - 7\delta + 1)M_{\rm b}^2 - (\delta+1)^3]\end{aligned}. \tag{B3}$$

It is straightforward to show that $\Delta_0 < 0$ if and only if $M_{\rm b} < M_{\rm crit}$, where $M_{\rm crit}$ is given by equation (22). Since the solution must converge to that of the incompressible sheet (equation 17) for $M_{\rm b} \ll 1$, and since this admits only two complex conjugate solutions, we deduce that the two real solutions to the quartic part of equation (20) at $M_{\rm b} < M_{\rm crit}$ are not solutions to the dispersion relation, $Z = 1$. Rather they must also be solutions to $Z = -1$, similar to the two solutions to the quadratic part. We discuss this further below.

For $M_{\rm b} > M_{\rm crit}$, we obtain $\Delta_0 > 0$ and the nature of roots depends on the signs of two additional parameters,

$$\Delta_1 = 8ac - 3b^2, \tag{B4}$$

$$\Delta_2 = 64a^3e - 16a^2c^2 + 16ab^2c - 16a^2bd - 3b^4. \tag{B5}$$

If both $\Delta_1 < 0$ and $\Delta_2 < 0$ when $\Delta_0 > 0$, then all four roots are real and distinct. Otherwise the four roots are two pairs of complex conjugates (Rees 1922). For the quartic part of equation (20), we have

$$\Delta_1 = -\frac{4M_{\rm b}^2\left(2 + \delta(2 + M_{\rm b}^2)\right)}{\delta^2} < 0, \tag{B6}$$

$$\Delta_2 = -\frac{16M_{\rm b}^2(1+\delta)(1+\delta+2\delta M_{\rm b}^2)}{\delta^4} < 0. \tag{B7}$$

Since Δ_1 and Δ_2 are always negative, all four roots are real when $M_{\rm b} > M_{\rm crit}$, and the sheet is stable.

When $M_{\rm b} \gg 1$, asymptotic solutions can be found for the quartic part of equation (20),

$$\varpi \simeq \pm\frac{1}{M_{\rm b}}, \quad 1 \pm \frac{1}{M_{\rm s}}, \tag{B8}$$

where $M_{\rm s} = \delta^{1/2}M_{\rm b}$. Note that all four of these solutions result in $q_{\rm b}$ and $q_{\rm s}$ that are purely imaginary.

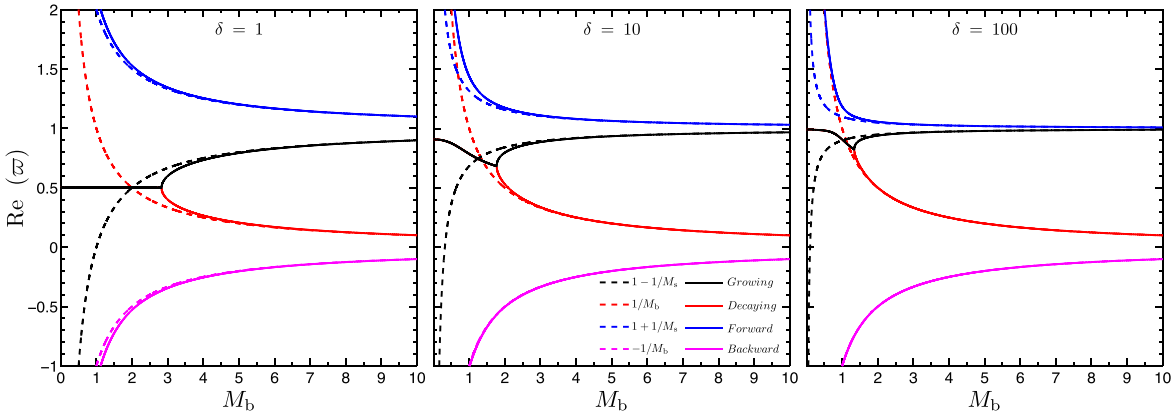

Figure B1. Real solutions to the quartic part of equation (20). We show Re(ϖ) as a function of M_b, for three different values of δ, as marked in the panels. Solid lines show numerical solutions. At low Mach numbers, two of the solutions are complex conjugates and therefore have the same real part, shown by the black solid line at low Mach numbers. These are the unstable growing and decaying mode, and the imaginary part is shown in Fig. 1. This line bifurcates into the solid black and red lines at the critical Mach number, M_crit from equation (22), above which the system becomes stable and these modes become independent travelling waves. The other four lines are stable travelling waves, which are not actually solutions to the dispersion relation $Z = 1$. The four dashed lines show the asymptotic high Mach number solutions from equation (B8). The fit is excellent in the entire stable regime.

When $\varpi = -M_\mathrm{b}^{-1}$ we have $\omega < 0$ and when $\varpi = 1 + M_\mathrm{s}^{-1}$ we have $\omega > kV$. Therefore, following the discussion in Appendix A, q_b and q_s will have the same sign, so $q_\mathrm{s}/q_\mathrm{b} > 0$ and $Z < 0$. Therefore, these cannot be solutions to $Z = 1$, but must yield $Z = -1$. We conclude that these are the high Mach number limits of the two roots that were real even for $M_\mathrm{b} < M_\mathrm{crit}$, which we already determined were not true solutions to the dispersion relation. The other two solutions, $\varpi = M_\mathrm{b}^{-1}$, $1 - M_\mathrm{s}^{-1}$, both result in $0 < \omega < kV$ and therefore $q_\mathrm{s}/q_\mathrm{b} < 0$ and $Z > 0$, meaning that $Z = 1$. Thus, these are the high Mach number limits of the true solutions to the dispersion relation.

In Fig. B1, we show numerical solutions to the quartic part of equation (20) as a function of Mach number, M_b, for different values of the density contrast, δ. For the two complex conjugates at low Mach numbers, representing the growing and decaying unstable modes, we show only the real part which is the same for both solutions (the complex part is shown in Fig. 1). At $M_\mathrm{b} > M_\mathrm{crit}$, these modes stabilize and become two independent travelling waves. This can be seen as the bifurcation point between the red and black lines in the figure. The other two solutions are always real, and can be thought of as a forward travelling wave with $\varpi > 0$ and a backward travelling wave with $\varpi < 0$. However, as discussed above, these are not solutions to the dispersion relation. At high Mach numbers, the four solutions to the quartic are well approximated by the asymptotic expressions in equation (B8), shown with dashed lines. These represent stable sound waves with phase velocities $\omega/k = v \pm c_\mathrm{s}, \pm c_\mathrm{b}$.

APPENDIX C: LONG-WAVELENGTH LIMIT OF THE COMPRESSIBLE SLAB

In this appendix, we derive the growth rate of the compressible slab in the long-wavelength limit, where $K \ll 1$. The first step is to verify that in this limit, $q_\mathrm{s}R_\mathrm{s} \ll 1$ as well, as this is what is needed to simplify the dispersion relation in equation (27). We accomplish this by showing that as $k \to 0$, $\omega \to 0$ as well. Otherwise, if $k = 0$ and $\omega \neq 0$, equation (12) reduces to $q_{\mathrm{b,\,s}} = \pm\mathrm{i}\omega/c_{\mathrm{b,\,s}}$. On the one hand, we are only interested in growing modes where Im(ω) > 0, and on the other hand we require Re($q_{\mathrm{b,\,s}}$) > 0. Therefore, we take $q_{\mathrm{b,\,s}} = -\mathrm{i}\omega/c_{\mathrm{b,\,s}}$. Inserting this into equation (25) yields

$$T\left(-\mathrm{i}\frac{\omega R_\mathrm{s}}{c_\mathrm{s}}\right) = -\delta^{-1/2}. \tag{C1}$$

Solving for ω results in

$$\omega = \frac{c_\mathrm{s}}{2R_\mathrm{s}}\left[-n\pi + \mathrm{iln}\left(\frac{\sqrt{\delta}-1}{\sqrt{\delta}+1}\right)\right], \tag{C2}$$

where n is any whole number, even for S-modes and odd for P-modes. For any $\delta > 0$, equation (C2) results in Im(ω) < 0, which is in contradiction to our original assumption. We conclude that there are no solutions with $\omega(k = 0) \neq 0$. Therefore, $q_{\mathrm{b,\,s}} \to 0$ as $k \to 0$, and $\tanh(q_\mathrm{s}R_\mathrm{s}) \simeq 1/\coth(q_\mathrm{s}R_\mathrm{s}) \simeq q_\mathrm{s}R_\mathrm{s}$. Inserting this into equation (27) yields

$$K = -\frac{\varpi^2}{\delta\,(\varpi-1)^2\left(1-M_\mathrm{b}^2\varpi^2\right)^{1/2}} \quad \text{(S)} \tag{C3a}$$

$$K = -\frac{\delta\,(\varpi-1)^2\left(1-M_\mathrm{b}^2\varpi^2\right)^{1/2}}{\varpi^2\left(1-\delta M_\mathrm{b}^2(\varpi-1)^2\right)} \quad \text{(P)}. \tag{C3b}$$

S-modes. The solution to equation (C3a) for $K = 0$ is $\varpi_0 = 0$. For $K \ll 1$, the lowest order correction is $\varpi_1 \simeq \pm\mathrm{i}\delta^{1/2}K^{1/2}$. To find the next-order correction, we insert $\varpi = \varpi_1 + \varpi_2$ with $\varpi_2 \ll \varpi_1 \ll 1$. This results in $\varpi_2 \simeq \delta K$, which is the leading-order term in Re(ϖ). Thus, at long wavelengths, S-modes are unstable with the approximate dispersion relation

$$\omega_{\mathrm{S,\,f}} \simeq \frac{V}{R_\mathrm{s}}\left[\delta K^2 \pm \mathrm{i}\delta^{1/2}K^{3/2}\right]. \tag{C4}$$

P-modes. When $K = 0$, there are two solutions to equation (C3b): $\varpi_0 = 1$ and $\varpi_0 = M_\mathrm{b}^{-1}$. In the vicinity of $\varpi_0 = 1$, the system is unstable. Inserting $\varpi = 1 + \varpi_1$ with $\varpi_1 \ll 1$ into equation (C3b) yields $\varpi_1 \simeq \pm\mathrm{i}K^{1/2}\delta^{-1/2}(1 - M_\mathrm{b}^2)^{-1/4}$. So at long wavelengths, P-modes are unstable with the approximate dispersion relation

$$\omega_{\mathrm{P,\,f}} \simeq \frac{V}{R_\mathrm{s}}\left[K \pm \mathrm{i}\delta^{-1/2}(1-M_\mathrm{b}^2)^{-1/4}K^{3/2}\right]. \tag{C5}$$

For the special case of $M_b = 1$, one gets instead $\varpi_1^{5/2} \simeq (iK)/(\sqrt{2}\delta)$ and the dispersion relation becomes, to lowest order in K,

$$\omega_{P,f} \simeq \frac{V}{R_s}\left[K \pm (-2\delta^2)^{-1/5} K^{7/5}\right]. \tag{C6}$$

When $M_b \neq 1$, the second solution to equation (C3b), $\varpi_0 = M_b^{-1}$, is stable. Inserting $\varpi = M_b^{-1}(1+\varpi_1)$ with $\varpi_1 \ll 1$ into equation (C3b) yields

$$\varpi_1 = -\frac{1}{2}\left[1 - \frac{1}{\delta(M_b-1)^2}\right]^2 K^2. \tag{C7}$$

APPENDIX D: SHORT-WAVELENGTH LIMIT OF THE COMPRESSIBLE SLAB

In this appendix, we discuss in detail the short-wavelength limit of the slab, where $K \gg 1$. There are two solutions to the dispersion relation, equations (28), for $K \to \infty$. These are $Z = 1$ and $1 - \delta M_b^2(\varpi - 1)^2 = 0$. However, care must be taken to ensure that K remains real, which must be the case in the temporal analysis we are discussing. By examining equations (28), we see that there are two different regimes, depending on the parameter

$$\gamma \equiv \frac{\mathrm{Im}\left(\sqrt{1-\delta M_b^2(\varpi-1)^2}\right)}{\mathrm{Re}\left(\sqrt{1-\delta M_b^2(\varpi-1)^2}\right)} = \frac{\mathrm{Im}(q_s)}{\mathrm{Re}(q_s)}. \tag{D1}$$

If $\gamma \ll 1$, then K will remain real as $Z \to 1$; in other words, the slab dispersion relation converges to that of the sheet at short wavelengths, as expected. In this case, q_s is very nearly real which means that these solutions represent *surface modes*, similar to the sheet. These decay exponentially with depth in the slab and prevent the two surfaces from coming into causal contact. We examine the regime of validity of this solution in Fig. D1, where we show the value of γ obtained for solutions to the sheet, i.e. $Z = 1$, as a function of M_b and δ. We see that $\gamma \ll 1$ only for low Mach numbers, $M_b \ll 1$. At $M_b \sim 1$, we have $\gamma \lesssim 1$ and the slab will deviate somewhat from the sheet solution of $Z = 1$ even at short wavelengths. As M_b approaches M_{crit} and the sheet becomes stable,

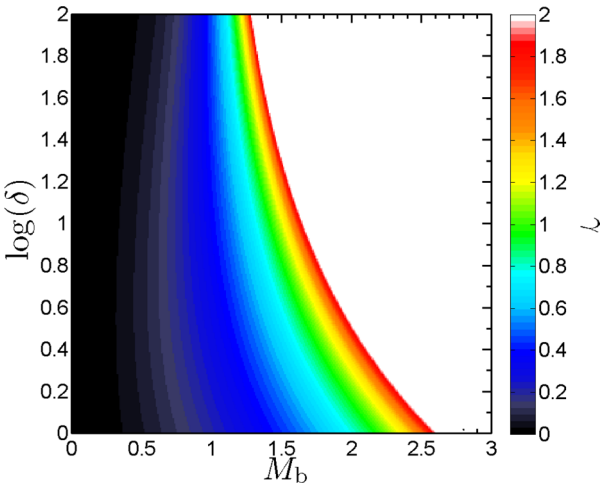

Figure D1. The value of $\gamma = \mathrm{Im}(q_s)/\mathrm{Re}(q_s)$ for the sheet solution. When $\gamma \ll 1$, the dispersion relation of the slab converges to that of the sheet, $Z = 1$, at short wavelengths. This happens only for low Mach numbers, $M_b \ll 1$. When $\gamma > 1$, which happens when the sheet is stable, the slab converges to the solution $\varpi = 1 - M_s^{-1}$, which is the high Mach number stable limit of the growing mode solution in the sheet.

q_s becomes purely imaginary and thus $\gamma > 1$, so $Z = 1$ is not a valid solution to the slab at short wavelengths.

When $\gamma \gg 1$, the short-wavelength limit of the slab is given by $1 - \delta M_b^2(\varpi - 1)^2 \to 0$. In this case, $\varpi \to \varpi_\infty \equiv 1 \pm 1/M_s$, which as we saw is the high Mach number asymptotic value of the growing mode solution in the sheet (equation B8). So either way, the slab converges to the sheet at short wavelengths. This leads to $Z \ll 1$, which ensures that K is real in equations (28). Such solutions have q_s that is very nearly imaginary which means that they represent *body modes*, which penetrate deep into the slab. In such a case, stable waves emanate from the interfaces and do not decay. These waves will be reflected off the slab boundaries, causing the two sides to come into causal contact.

APPENDIX E: STABILITY AND MARGINAL STABILITY IN THE SLAB

In this appendix, we analytically find all stable solutions to the slab dispersion relation, i.e. solution to equations (28) where both K and ϖ are real. This is a preliminary step towards finding the *marginally stable points* of the system. These are points in (ϖ, K) space where both parameters are real, but in the vicinity of which one or both of them become complex. In our temporal analysis, K is real by definition, so a marginally stable point is a stable solution where an infinitesimal change in K results in complex ϖ, which must correspond to an extremal point of the function $K(\varpi)$, where ϖ is real. To see this, consider a solution with $\varpi = 0, K(0)$, and imagine increasing K (decreasing the wavelength λ). So long as $K(\varpi)$ is monotonic, there is still a solution with real ϖ, and therefore the solution remains stable. But when $K(\varpi)$ reaches an extremal point, decreasing the wavelength further requires extending ϖ to the complex plane, indicating an instability (Fig. E1, discussed below).

There are two main branches of stable solutions, depending on whether q_s is real or imaginary. We will address each of these separately, as they define different families of solutions, for low and high Mach numbers.

E1 $q_s \in R \Rightarrow 1 - \delta M_b^2(1-\varpi)^2 > 0$

Such solutions represent surface waves that decay exponentially within the slab, with a penetration depth of q_s^{-1}. Such modes behave similarly to the sheet at short wavelengths since the two sides of the slab are not in contact with each other (Appendix D). For K to be real, we require

$$K = \mathrm{Re}(K) = \frac{\ln(|1+Z|) - \ln(|1-Z|)}{2\sqrt{1-\delta M_b^2(\varpi-1)^2}}, \tag{E1a}$$

$$\mathrm{Im}(K) = \frac{\arg(1+Z) - \arg(1-Z) + n\pi}{2\sqrt{1-\delta M_b^2(\varpi-1)^2}} = 0. \tag{E1b}$$

If $q_b \in \boldsymbol{R}$, then $1 - M_b^2\varpi^2 \geq 0$ and $Z = -|Z|$ is on the negative real axis. If $|Z| \leq 1$, then $\arg(1+Z) = 0$ and equation (E1b) can be satisfied with $n = 0$. If $|Z| > 1$, then $\arg(1+Z) = \pi$ and equation (E1b) can be satisfied with $n = -1$. Either way, equation (E1a) results in $K \leq 0$. Physically, we require $K = |k|R_s \geq 0$, so the only relevant solutions in this case are those with $K = 0$. If $n = 0$, then $-1 \leq Z \leq 0$, so $K = 0$ is only possible for $Z = 0$. Since we have assumed here $q_s > 0$, this in turn requires $\varpi = 0$, which corresponds to the fundamental S-mode (Appendix C). If $n = -1$, then $Z < -1$, so $K = 0$ is only possible for $Z = -\infty$. This in turn requires $\varpi = 1$ (or M_b^{-1}), which corresponds to the fundamental P-mode

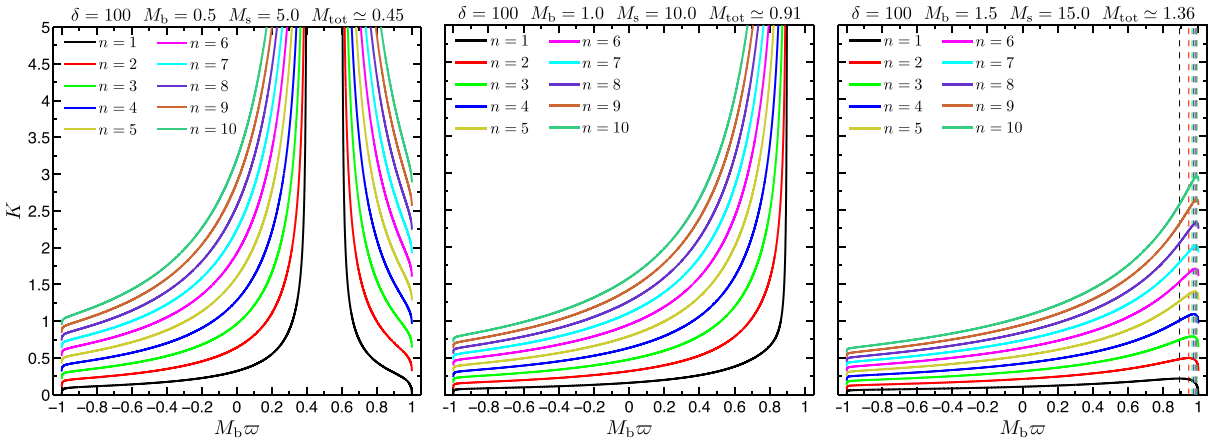

Figure E1. The first 10 modes of equation (E3), for three different regimes of M_b. The left-hand panel represents low Mach numbers, $M_\mathrm{b} < 1 - 1/\sqrt{\delta}$, and the middle panel represents intermediate Mach numbers, $1 - 1/\sqrt{\delta} < M_\mathrm{b} < 1 + 1/\sqrt{\delta}$. In both these cases, there are no marginally stable points and each mode is stable at all wavelengths. The right-hand panel represents high Mach numbers, $1 + 1/\sqrt{\delta} < M_\mathrm{b}$, where the flow is supersonic with respect to the sum of the two sound speeds $M_\mathrm{tot} = v/(c_\mathrm{b} + c_\mathrm{s}) > 1$. In this case, each $K(\varpi)$ curve has a maximum in the range $0 < \varpi < M_\mathrm{b}^{-1}$, marked with a dashed line. These maxima, K_n, represent marginally stable points, since increasing K beyond K_n introduces an imaginary component to ϖ and triggers an instability.

(Appendix C). Recall that at $K = 0$, the system is unstable for $\varpi = 0$ and 1, but stable for $\varpi = M_\mathrm{b}^{-1}$ (Appendix C).

Note that our assumptions above, whereby $q_\mathrm{s} > 0$ and $q_\mathrm{b} \geq 0$, limit the range of ϖ to $1 - M_\mathrm{s}^{-1} < \varpi < 1 + M_\mathrm{s}^{-1}$ and $-M_\mathrm{b}^{-1} \leq \varpi \leq M_\mathrm{b}^{-1}$. The solutions $\varpi = 0,\ 1,\ M_\mathrm{b}^{-1}$ are only included in this range at low Mach numbers: $M_\mathrm{s} < 1$, $M_\mathrm{b} \leq 1$ and $1 - 1/\sqrt{\delta} < M_\mathrm{b} < 1 + 1/\sqrt{\delta}$, respectively.

On the other hand, if $q_\mathrm{b} \in \boldsymbol{I}$ so that $1 - M_\mathrm{b}^2\varpi^2 < 0$, then $q_\mathrm{b} = -\mathrm{i}|q_\mathrm{b}|$ and $Z = -\mathrm{i}|Z|$ is on the negative imaginary axis. Therefore, $-\pi/2 \leq \arg(1 \pm Z) \leq \pi/2$ and equation (E1b) can be satisfied with $n = 0$ only if $Z = 0$, which would require $\varpi = 0$, in contradiction to the assumption that $1 - M_\mathrm{b}^2\varpi^2 < 0$. A solution with $n = -1$ is possible if $|Z| = \infty$ so that $(1 + Z)/(1 - Z) = -1$. In this case, provided $M_\mathrm{b} > 1$, the solution is $K = 0$ and $\varpi = 1$, corresponding to the unstable fundamental (P) mode. The solution $\varpi = M_\mathrm{b}^{-1}$ is in contradiction to the assumption that $1 - M_\mathrm{b}^2\varpi^2 < 0$.

E2 $q_\mathrm{s} \in \boldsymbol{I} \Rightarrow 1 - \delta M_\mathrm{b}^2(1 - \varpi)^2 < 0$

Such solutions represent waves that do not decay spatially within the slab. They travel from one interface to the other and are reflected off of and transmitted through the slab boundaries. These are *body modes* or *reflected modes*. In this case, since the two sides of the slab can interact with each other through the reflection of waves, the slab will differ greatly from the sheet. In this regime $q_\mathrm{s} = \mathrm{i}|q_\mathrm{s}|$ (Appendix A) and ϖ must obey either $1 + M_\mathrm{s}^{-1} < \varpi$ or $\varpi < 1 - M_\mathrm{s}^{-1}$. For K to be real, we require

$$K = \mathrm{Re}(K) = \frac{\arg(1 + Z) - \arg(1 - Z) + n\pi}{2\sqrt{\delta M_\mathrm{b}^2(\varpi - 1)^2 - 1}}, \tag{E2a}$$

$$\mathrm{Im}(K) = -\frac{\ln(|1 + Z|) - \ln(|1 - Z|)}{2\sqrt{\delta M_\mathrm{b}^2(\varpi - 1)^2 - 1}} = 0. \tag{E2b}$$

If $q_\mathrm{b} \in \boldsymbol{I}$ so that $1 - M_\mathrm{b}^2\varpi^2 < 0$, then $q_\mathrm{b} = -\mathrm{i}|q_\mathrm{b}|$ (Appendix A) and $Z = +|Z|$ is on the positive real axis. Equation (E2b) can thus only be satisfied if $Z = 0$, which requires $\varpi = 0$, which is in contradiction to the assumption that $1 - M_\mathrm{b}^2\varpi^2 < 0$. We therefore conclude that no such solution exists.

On the other hand, if $q_\mathrm{b} \in \boldsymbol{R}$ so that $1 - M_\mathrm{b}^2\varpi^2 \geq 0$, then $Z = -\mathrm{i}|Z|$ is on the negative imaginary axis. In this case, $1 - Z = 1 + \bar{Z}$ and equation (E2b) is always satisfied. Furthermore, equation (E2a) can be rewritten as

$$K = \frac{-\arctan(|Z|) + (n/2)\pi}{\sqrt{\delta M_\mathrm{b}^2(\varpi - 1)^2 - 1}}. \tag{E3}$$

For $n < 0$, equation (E3) always results in $K < 0$, which is not relevant for our discussion. For $n = 0$, equation (E3) results in $K \leq 0$ so the only relevant solution is $K = 0$, which requires $|Z| = 0$, which in turn requires $\varpi = 0$. Provided $M_\mathrm{s} > 1$, this corresponds to the fundamental S-mode.

For $n \geq 1$, equation (E3) results in $K \geq 0$ for all ϖ. However, our assumptions of $q_\mathrm{s}^2 < 0$ and $q_\mathrm{b}^2 \geq 0$ limit the range of allowed ϖ values to $-M_\mathrm{b}^{-1} \leq \varpi \leq M_\mathrm{b}^{-1}$ and either $1 + M_\mathrm{s}^{-1} < \varpi$ or $\varpi < 1 - M_\mathrm{s}^{-1}$. For the nth mode, $\varpi = 0$ when $K = K_{\mathrm{n},0} = n\pi/(2\sqrt{M_\mathrm{s}^2 - 1})$, provided $M_\mathrm{s} > 1$.

In Fig. E1, we show K as a function of $(M_\mathrm{b}\varpi)$ from equation (E3), for $n = 1$–10. The three panels are representative of three different regimes of Mach number. The left-hand panel represents low Mach numbers, $M_\mathrm{b} < 1 - 1/\sqrt{\delta}$, corresponding to flow velocities of $v < c_\mathrm{b} - c_\mathrm{s}$. In this case, both branches of ϖ are accessible. $K(\varpi)$ increases monotonically from $\varpi = -M_\mathrm{b}^{-1}$ until $\varpi = 1 - M_\mathrm{s}^{-1}$ where $K \to \infty$. It then decreases monotonically from $\varpi = 1 + M_\mathrm{s}^{-1}$, where again $K \to \infty$, until $\varpi = M_\mathrm{b}^{-1}$. The centre panel represents intermediate Mach numbers, $1 - 1/\sqrt{\delta} < M_\mathrm{b} < 1 + 1/\sqrt{\delta}$, corresponding to flow velocities $c_\mathrm{b} - c_\mathrm{s} < v < c_\mathrm{b} + c_\mathrm{s}$. In this case, only $\varpi < 1 - M_\mathrm{s}^{-1}$ is accessible, but the qualitative behaviour of $K(\varpi)$ in this regime is the same as in the previous case, shown in the left-hand panel. In both these cases, there are *no* marginally stable points with $K > 0$. Solutions with $n \geq 1$ are stable at all wavelengths. Once the nth mode has been excited, at $K = K_{\mathrm{n},0}$, we can increase K (decrease the wavelength) continuously, and there will always be a solution to the mode with real ϖ. Since we never require complex ϖ, no instability is ever triggered.

The right-hand panel of Fig. E1 represents large Mach numbers, $1 + 1/\sqrt{\delta} < M_\mathrm{b}$, corresponding to flow velocities which are supersonic with respect to the sum of the two sound speeds: $v > c_\mathrm{b} + c_\mathrm{s} \Rightarrow M_\mathrm{tot} > 1$. In this case, the $K(\varpi)$ curve

corresponding to each mode has exactly one maximum point in the range $0 < \varpi < M_{\rm b}^{-1}$, as shown in the figure. We refer to these maxima as $K_{\rm n}$ and $\varpi_{\rm n}$. *These are marginally stable points*.

APPENDIX F: MARGINALLY STABLE POINTS FOR LARGE *n*

The marginally stable points are given by $\mathrm{d}K/\mathrm{d}\varpi = 0$ with $K(\varpi)$ given by equation (E3). This equation cannot be solved analytically in general, but in this appendix we derive an analytical approximation for large n.

Based on the discussion in the previous appendix, when $M_{\rm tot} > 1$, equation (E3) is continuous in the range $-M_{\rm b}^{-1} \leq \varpi \leq M_{\rm b}^{-1}$. Since $0 \leq \arctan(|Z|) \leq \pi/2$, for $n \gg 1$ equation (E3) can be approximated as $K \simeq (n\pi/2)(\delta M_{\rm b}^2(\varpi - 1)^2 - 1)^{-1/2}$, which is a monotonically increasing function of ϖ. We conclude that for $n > 1$, $\varpi_{\rm n}$ converges to $M_{\rm b}^{-1}$ (see the right-hand panel of Fig. E1). When $\varpi = M_{\rm b}^{-1}$ we get $|Z| = \infty$, so for $\varpi_{\rm n} = M_{\rm b}^{-1}(1 - \mathcal{W})$, with $0 < \mathcal{W} \ll 1$, we have $|Z| \gg 1$ and $\arctan(|Z|) = \pi/2 - |Z|^{-1} + O(|Z|^{-3})$. To leading order in $\mathcal{W}$,

$$|Z|^{-1} \simeq \frac{\sqrt{2}\delta(M_{\rm b}-1)^2}{\sqrt{\delta(M_{\rm b}-1)^2 - 1}}\mathcal{W}^{1/2}. \tag{F1}$$

In order to find $K_{\rm n}$, the maximum of equation (E3), we expand K to the second leading order in $\mathcal{W}$:

$$K \simeq K_0 + K_1\mathcal{W}^{1/2} + K_2\mathcal{W}, \tag{F2a}$$

$$K_0 = \frac{n\pi}{2\sqrt{\delta(M_{\rm b}-1)^2 - 1}}, \tag{F2b}$$

$$K_1 = \frac{\sqrt{2}\delta(M_{\rm b}-1)^2}{\delta(M_{\rm b}-1)^2 - 1}, \tag{F2c}$$

$$K_2 = \frac{n\pi\delta(M_{\rm b}-1)}{2\left(\delta(M_{\rm b}-1)^2 - 1\right)^{3/2}}. \tag{F2d}$$

It is now straightforward to find the maximum of equations (F2), which approximates the marginally stable point of the nth mode

$$\mathcal{W}_{\rm n} \simeq \frac{2\,(M_{\rm b}-1)^2\left[\delta\,(M_{\rm b}-1)^2 - 1\right]}{n^2\pi^2}, \tag{F3a}$$

$$K_{\rm n} \simeq \frac{n\pi}{2\sqrt{\delta(M_{\rm b}-1)^2 - 1}}. \tag{F3b}$$

$\varpi_{\rm n}$ thus converges to $M_{\rm b}^{-1}$ as n^{-2} while $K_{\rm n}$ grows linearly with n.

To ensure $\varpi_{\rm n} \leq M_{\rm b}^{-1}$, we require $\mathcal{W}_{\rm n} \geq 0$. From equation (F3a), this leads to

$$M_{\rm b}^{-1} + M_{\rm s}^{-1} \leq 1 \Rightarrow v \geq c_{\rm b} + c_{\rm s}. \tag{F4}$$

This supports what was inferred from Fig. E1 in Appendix E, namely that marginally stable points exist only for flows that are supersonic with respect to the sum of the two sound speeds. All we assumed in deriving equations (F3) was that $K(\varpi)$ from equation (E3) was continuous for $|\varpi| \leq M_{\rm b}^{-1}$, which requires only $v \geq c_{\rm b} - c_{\rm s}$. Such a flow is not necessarily supersonic at all, while the existence of unstable modes with $n \geq 1$ is a purely supersonic effect.

Our approximation for $\mathcal{W}_{\rm n}$ is only valid if $|Z|^{-1} \ll \pi/2$, with $|Z|^{-1}$ given in equation (F1). It is straightforward to verify that this condition also guarantees $\mathcal{W}_{\rm n} \ll 1$ in equation (F3a). The value of n for which $|Z|^{-1} \simeq 1$ is

$$n_1 \simeq \delta\,(M_{\rm b}-1)^3\,. \tag{F5}$$

We expect equations (F3) to converge for $n \gg n_1$.

In Fig. F1, we compare equations (F3) to exact numerical solutions for the maxima of equation (E3), for different values of $M_{\rm b}$ and δ. The left-hand panel shows $K_{\rm n}$ and the right-hand panel shows $\mathcal{W}_{\rm n}$. The approximation for $K_{\rm n}$ improves with increasing n and increasing $M_{\rm tot}$. For $M_{\rm tot} \gtrsim 2$, the error is less than 10 per cent already for $n \gtrsim 2$, while for lower $M_{\rm tot}$ this error is achieved for $n \gtrsim 10$. On the other hand, the approximation for the marginally stable frequency, equation (F3a), only converges for $n > n_1$ as expected

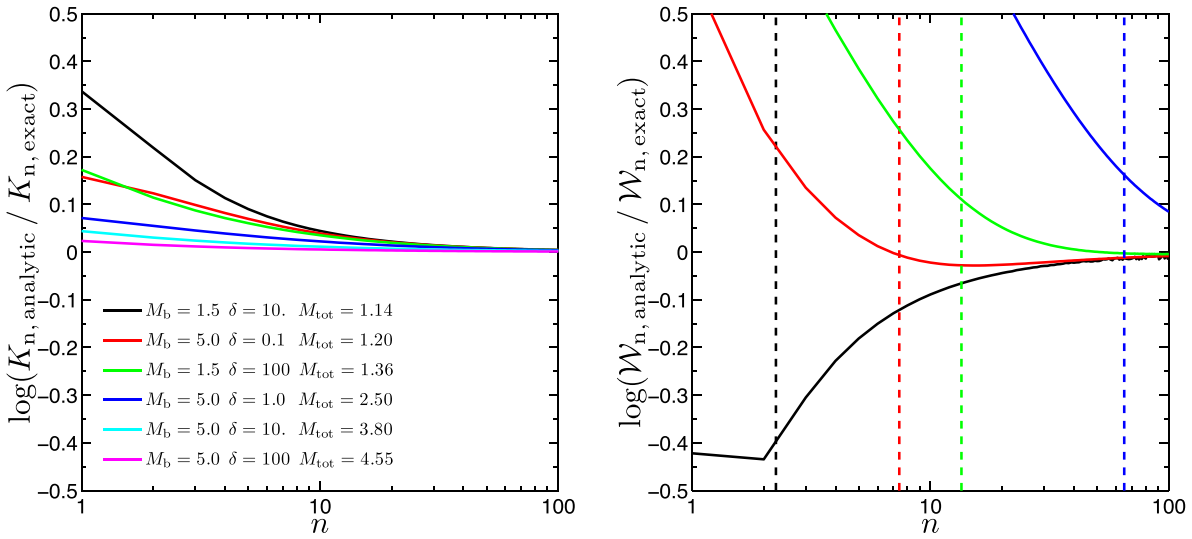

Figure F1. Comparison of our analytic approximation for the marginally stable points from equations (F3), with the exact solution obtained by numerically finding the maxima of equation (E3). The left-hand panel compares $K_{\rm n}$ and the right-hand panel compares $\mathcal{W}_{\rm n}$. Solid lines show the log of the ratio of the analytic estimate to the numerical solution for different combinations of $M_{\rm b}$ and δ, corresponding to different values of $M_{\rm tot}$. In all cases examined, there is less than 10 per cent error in the approximation for $K_{\rm n}$ by $n \sim 10$, and for $M_{\rm tot} \gtrsim 2$ this is the case already at $n \sim 2$. On the other hand, the approximation for $\mathcal{W}_{\rm n}$ converges only for $n > n_1$ (equation F5, dashed lines), which increases rapidly with $M_{\rm tot}$. The curves with $M_{\rm tot} = 3.80$ and 4.55 lie outside the bounds of the panel, converging only at very high n.

(equation F5). Unfortunately, for even moderately high Mach numbers and density contrasts, n_1 can be quite high. For example, for $M_b = 5$ and $\delta = 1$, $n_1 \simeq 65$.

Modes with $n \geq 1$ begin stable at $K = K_{n,0}, \varpi = 0$, pass through marginal stability at $K = K_n$, $\varpi \simeq M_b^{-1}$ and end at $K = \infty$, $\varpi_\infty = 1 - M_s^{-1}$. As a result, $|Z|$ begins near 0, reaches large values $|Z| \gg 1$ and ends near 0 again. Therefore, $(1 + Z)/(1 - Z)$ goes from ~ 1 to ~ -1 and back to ~ 1, completing a full revolution about the origin in the complex plane. This is the reason for the extra 2π in equation (31) compared to equations (28).

APPENDIX G: GROWTH RATES NEAR MARGINAL STABILITY

Using our approximation for the behaviour of $K(\varpi)$ near marginal stability (equations F2), we can derive the growth rate of the nth mode. We assume $K = K_n + \kappa$ and $\varpi = M_b^{-1}(1 - \mathcal{W}_n + \xi)$, with $\kappa \ll K_n$ and $|\xi| \ll \mathcal{W}_n \ll 1$. By inserting this into equations (F2), we obtain to leading order in κ

$$\xi \simeq \pm \mathrm{i} \left[\frac{8 M_b^{3/2} \left[\delta (M_b - 1)^2 - 1 \right]}{\sqrt{2} \delta (M_b - 1)^2} \mathcal{W}_n^{3/2} \right]^{1/2} \kappa^{1/2}. \tag{G1}$$

This shows that the system is indeed unstable near K_n, and that this instability has a growing mode. Using our approximation for $\mathcal{W}_n$ from equation (F3a), equation (G1) becomes

$$\xi \simeq \pm \mathrm{i} \frac{8 \sqrt{(M_b - 1)} \left[\delta (M_b - 1)^2 - 1 \right]^{5/4}}{\sqrt{\delta} \left[n\pi \right]^{3/2}} \kappa^{1/2}. \tag{G2}$$

The growth rate near marginal stability is

$$\mathrm{Im}(\omega) = k v \, \mathrm{Im}(\varpi) = k c_b |\xi|. \tag{G3}$$

ξ can be computed either from equation (G1) using the exact (numerical) solution for $\mathcal{W}_n$ or from equation (G2) using our analytic approximation, which we saw to be a good approximation for $n > n_1$ (equation F5).

The analytic approximation for ξ is compared to numerical solutions of the dispersion relation in Fig. G1, for different values of δ and M_b. The coloured lines show the result of a full numerical solution to the dispersion relation (equation 27) for the modes $n = 1$–40. The dashed black line is the analytic approximation. We show $\xi = \mathrm{Im}(\varpi)$, normalized by the n-dependent prefactor of $\kappa^{1/2}$ in equation (G1), as a function of κ. When computing ξ and κ from equation (G1), we used the numerical results for $\mathcal{W}_n$ and K_n, obtained by finding the maximum of $K(\varpi)$ in equation (E3). Though not fully analytic, this is still much easier to evaluate numerically than a full solution to the dispersion relation, and is thus still useful. In all cases examined, the scaling of $\xi \propto \kappa^{1/2}$ is captured at $\kappa \lesssim 0.1$ for all n, even if the normalization has not yet converged. The normalization converges rapidly as well for low Mach numbers (left-hand panel), though more slowly for high Mach numbers, qualitatively similar to the convergence of equation (F3a) for $\mathcal{W}_n$ (Fig. F1).

For high Mach numbers, $M_b \gg 1$, equation (G2) yields $\xi \propto \delta^{3/4} M_b^3 n^{-3/2}$ (for $n > n_1$), while $k \simeq K_n \propto \delta^{-1/2} M_b^{-1} n$. The growth rate near marginal stability thus scales as

$$\mathrm{Im}(\omega) \propto \delta^{1/4} M_b^2 n^{-1/2}. \tag{G4}$$

The scaling of M_b^2 is very different from the growth rate near marginal stability for the fundamental modes. For the S-mode, this is independent of M_b (equation C4), and for the P-mode it scales as $M_b^{-1/2}$ (equation C5).

APPENDIX H: FASTEST GROWING MODE IN THE SLAB

For each mode, the growth rate is zero at marginal stability, grows larger as K is increased and then goes to zero again at $K \to \infty$ (Appendix D). Each mode thus has a maximal growth rate at some intermediate K, hereafter the *resonance* of the mode. It is of particular interest to estimate this maximal growth rate, and how it scales with mode number n, or alternatively with wavenumber K. This will tell us which mode is dominant for perturbations of a particular wavelength, and will give an estimate of the fastest growth rate. Below, we derive an analytic approximation for the maximal growth rate which is valid for very supersonic flows, $M_{tot} = v/(c_b + c_s) \gg 1$ (though in practice, it is a good approximation for $M_{tot} \gtrsim 1.5$).

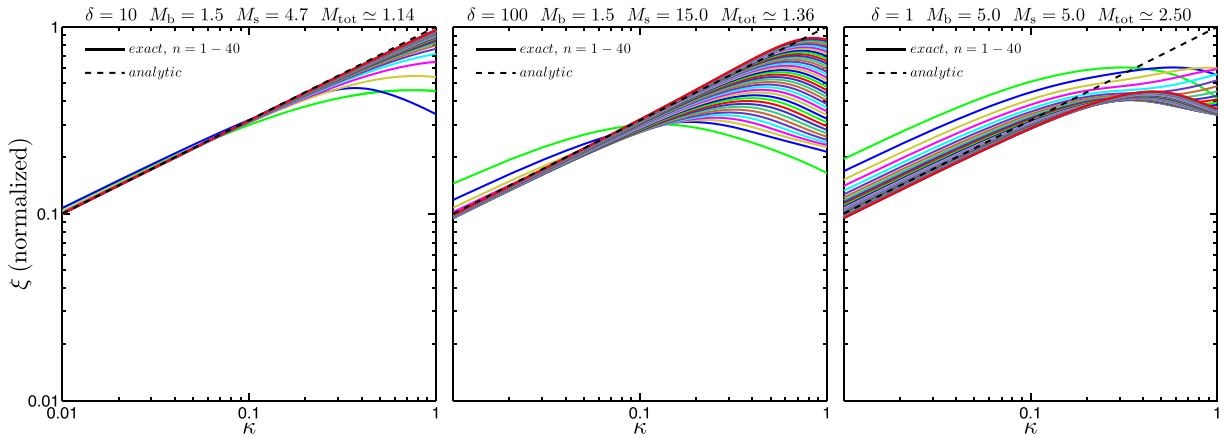

Figure G1. Comparison of our analytic estimate for the growth rate of modes with $n \geq 1$ near marginal stability to a numerical solution of the dispersion relation. The x-axis is $\kappa = K - K_n$, the wavenumber relative to marginal stability. The y-axis is $\xi = \mathrm{Im}(\varpi)$, normalized by the n-dependent factor multiplying $\kappa^{1/2}$ in equation (G1). We used the exact value for K_n and $\mathcal{W}_n$ when computing κ and ξ, obtained by numerically finding the maximum of $K(\varpi)$ in equation (E3). The black dashed line shows the analytic prediction and the coloured solid lines show numerical calculations of the first 40 modes, $n = 1$–40, increasing from top to bottom. For all cases examined, the slope of $\xi \propto \kappa^{1/2}$ is reproduced at $\kappa \lesssim 0.1$. Increasing n or decreasing M_{tot} makes the slope a good fit at higher κ as well, and improves the fit to the normalization of ξ. However, even at high M_{tot}, the normalization is well approximated by equation (G1) by $n \sim 5$.

We make two additional assumptions. The first is that ϖ is sufficiently far from both 0 and 1 at resonance, so that $\delta M_{\rm b}(\varpi-1)^2 \gg 1$ and $M_{\rm b}\varpi^2 \gg 1$. The second is that the growth rate at resonance is much smaller than the angular frequency. In other words, if $\omega = \omega_{\rm R} + {\rm i}\omega_{\rm I}$, then $\omega_{\rm I} \ll \omega_{\rm R}$ at resonance. We empirically show these two assumptions to be valid by numerically solving the dispersion relation (see Fig. 4). However, they can both be justified analytically as well. When $M_{\rm tot} \gg 1$, ϖ grows from $\lesssim M_{\rm b}^{-1} \sim 0$ at marginal stability to $1 - M_{\rm s}^{-1} \sim 1$ as $K \to \infty$. Since in both of these limits the growth rate goes to zero, it is reasonable to assume that resonance occurs far from these points, so that ϖ is sufficiently far from both 0 and 1. The second assumption can be justified by realizing that while both $\varpi_{\rm R}$ and $\varpi_{\rm I}$ start very small at marginal stability, $\varpi_{\rm R}$ increases monotonically to an asymptotic value of $\sim$1, while $\varpi_{\rm I}$ flattens, reaches a maximum at resonance and then decays to zero. It is therefore reasonable to assume that $\varpi_{\rm I} \ll \varpi_{\rm R}$ at resonance, and therefore that $\omega_{\rm I} \ll \omega_{\rm R}$.

Using these assumptions, and the fact that in our chosen branch cut ${\rm Re}(q_{\rm b,\,s}) > 0$, ${\rm Im}(q_{\rm b}) < 0$, ${\rm Im}(q_{\rm s}) > 0$ (Appendix A), we have $q_{\rm b} = \sqrt{1 - M_{\rm b}^2\varpi^2} \simeq -{\rm i}M_{\rm b}\varpi$ and $q_{\rm s} = \sqrt{1 - \delta M_{\rm b}^2(1-\varpi)^2} \simeq {\rm i}\sqrt{\delta}M_{\rm b}(1-\varpi)$. Inserting this into equation (18) yields

$$Z \simeq \frac{\varpi}{\sqrt{\delta}(1-\varpi)}. \tag{H1}$$

Writing $\varpi = \varpi_{\rm R} + {\rm i}\varpi_{\rm I}$ and $(1+Z)/(1-Z) = A\,{\rm e}^{{\rm i}\theta}$, we obtain from equation (28)

$$\varpi_{\rm R} \simeq 1 - \frac{\theta + n\pi}{2\sqrt{\delta}M_{\rm b}K}, \tag{H2a}$$

$$\varpi_{\rm I} \simeq \frac{1}{2\sqrt{\delta}M_{\rm b}K}\ln(A) \Rightarrow \omega_{\rm I} \simeq \frac{c_{\rm s}}{2R_{\rm s}}\ln(A). \tag{H2b}$$

We thus conclude that resonance occurs at the maximum of A. After some algebra, it is straightforward to show from equation (H1) that

$$A^2 = \left|\frac{1+Z}{1-Z}\right|^2 \simeq \frac{\left[\varpi_{\rm R}(\sqrt{\delta}-1) - \sqrt{\delta}\right]^2 + \left[\varpi_{\rm I}(\sqrt{\delta}-1)\right]^2}{\left[\varpi_{\rm R}(\sqrt{\delta}+1) - \sqrt{\delta}\right]^2 + \left[\varpi_{\rm I}(\sqrt{\delta}+1)\right]^2}. \tag{H3}$$

Neglecting terms of order $(\varpi_{\rm I}/\varpi_{\rm R})^2 \ll 1$, the maximum of A occurs when

$$\varpi_{\rm R,\,res} \simeq \frac{\sqrt{\delta}}{\sqrt{\delta}+1} = \frac{c_{\rm b}}{c_{\rm b}+c_{\rm s}}, \tag{H4a}$$

$$A_{\rm res} \simeq \frac{2\sqrt{\delta}}{\varpi_{\rm I,\,res}\left(\sqrt{\delta}+1\right)^2}. \tag{H4b}$$

Neglecting terms of order $\varpi_{\rm I}/\varpi_{\rm R}$, we have $|q_{\rm b}| \simeq |q_{\rm s}|$ at resonance. This means that the perturbation penetrates the same depth into the slab as into the background. It also means that the angle of propagation relative to the normal to the slab, given by

$$\cot\left(\Psi_{\rm b,s}\right) = \frac{\left|{\rm Im}(q_{\rm b,s})\right|}{k}, \tag{H5}$$

is the same within the slab and the background. At resonance, the angle is

$$\sin\left(\Psi_{\rm res}\right) \simeq \frac{\sqrt{\delta}+1}{\sqrt{\delta}M_{\rm b}} = \frac{1}{M_{\rm tot}}, \tag{H6}$$

where in the last equality we have used $M_{\rm tot}^{-1} = M_{\rm b}^{-1} + M_{\rm s}^{-1}$. This is commonly referred to as the *Mach angle*.

Inserting equation (H4b) into equation (H2b) gives an estimate for the growth rate at resonance

$$t_{\rm sc}\omega_{\rm I,\,res} + \ln\left(t_{\rm sc}\omega_{\rm I,\,res}\right) \simeq \ln\left(4M_{\rm tot}\frac{\sqrt{\delta}}{1+\sqrt{\delta}}K_{\rm res}\right), \tag{H7}$$

where $t_{\rm sc} = 2R_{\rm s}/c_{\rm s}$ is the sound-crossing time in the slab. The solution to this equation can be expressed as an infinite sequence of functions

$$t_{\rm sc}\omega_{\rm I,\,1} = \ln\left(4M_{\rm tot}\frac{\sqrt{\delta}}{1+\sqrt{\delta}}K\right), \tag{H8a}$$

$$t_{\rm sc}\omega_{\rm I,\,j} = t_{\rm sc}\omega_{\rm I,\,1} - \ln\left(t_{\rm sc}\omega_{\rm I,\,j-1}\right). \tag{H8b}$$

As $K \to \infty$, the sequence converges to $\omega_{\rm I,\,1}$ and in practice, it converges to $\omega_{\rm I,\,3}$ even for small K. The growth rate at resonance diverges logarithmically with wavenumber, $\omega_{\rm I} \propto \ln(k)$. As shown in Fig. 4, this is the effective growth rate for the slab, since at each wavenumber the growth rate will be dominated by the mode closest to resonance. This should be compared to the case of the incompressible slab and the compressible/incompressible sheet. In the incompressible cases, the system is always unstable and the growth rate diverges linearly with wavenumber, $\omega_{\rm I} \propto k$. In the compressible sheet, the same scaling applies at low Mach numbers, while at high Mach numbers the system is stable, $\omega_{\rm I} = 0$. The scaling of $\omega_{\rm I} \propto \ln(k)$ for the effective growth rate in the compressible slab can be seen as a 'compromise' between these two extremes, diverging at short wavelengths, but only logarithmically. Also, recall that it is only the effective growth rate, comprised of the fastest growing modes at each wavelength, which diverges. Each individual mode stabilizes as $k \to \infty$, as discussed in Appendix D.

By inserting equation (H4a) into equation (H2a), we can estimate the wavenumber at resonance. Neglecting terms of order $\theta = O(\varpi_{\rm I}/\varpi_{\rm R})$

$$K_{\rm res} \simeq \frac{n\pi}{2M_{\rm tot}}. \tag{H9}$$

The resonant wavenumber increases linearly with n, similar to the marginally stable wavenumber (equation F3b). When $M_{\rm tot} \gg 1$, $K_{\rm res}$ is very nearly continuous.

Figs H1 and H2 compare our analytic approximations for the resonant frequency and wavelength to numerical solutions of the dispersion relation, for the first 40 modes, n = 1–40, for different values of δ and $M_{\rm b}$. The left-hand panel of Fig. H1 shows the resonant wavenumber, $K_{\rm res}$ (equation H9), the right-hand panel shows the phase velocity at resonance, $\varpi_{\rm R,\,res}$ (equation H4a) and Fig. H2 shows the growth rate at resonance, $\omega_{\rm I,\,res}$ (equation H8). In the left-hand panel of Fig. H2, we focus on one example, $M_{\rm b} = 1.5$ and $\delta = 100$, and examine the convergence of the sequence given in equation (H8), which is shown to converge by $\omega_{\rm I,\,3}$. In the right-hand panel, we compare $\omega_{\rm I,\,3}$ to numerical solutions for the same values of $M_{\rm b}$ and δ as in Fig. H1.

The fit to $\varpi_{\rm R,\,res}$ at resonance is good in all cases, with an error of less than $\lesssim$10 per cent. On the other hand, the approximations for $K_{\rm res}$ and $\omega_{\rm I,\,res}$ are quite poor at low Mach numbers, $M_{\rm tot} \lesssim 1.3$, but rapidly improve as $M_{\rm tot}$ is increased. The error in $\omega_{\rm I,\,res}$ reaches $\lesssim$10 per cent for $M_{\rm tot} \gtrsim 1.3$, and for $K_{\rm res}$ a similar error is achieved for $M_{\rm tot} \gtrsim 2$. This is expected, since the approximations we made are strictly valid for very high Mach numbers only. We note that in the cases where the approximation is particularly poor, $M_{\rm b} = 1.5$, $\delta = 10$ and $M_{\rm b} = 5.0$, $\delta = 0.1$, the sheet is still unstable since $M_{\rm b} < M_{\rm crit}$, so the slab instability is dominated by surface modes rather than body modes.

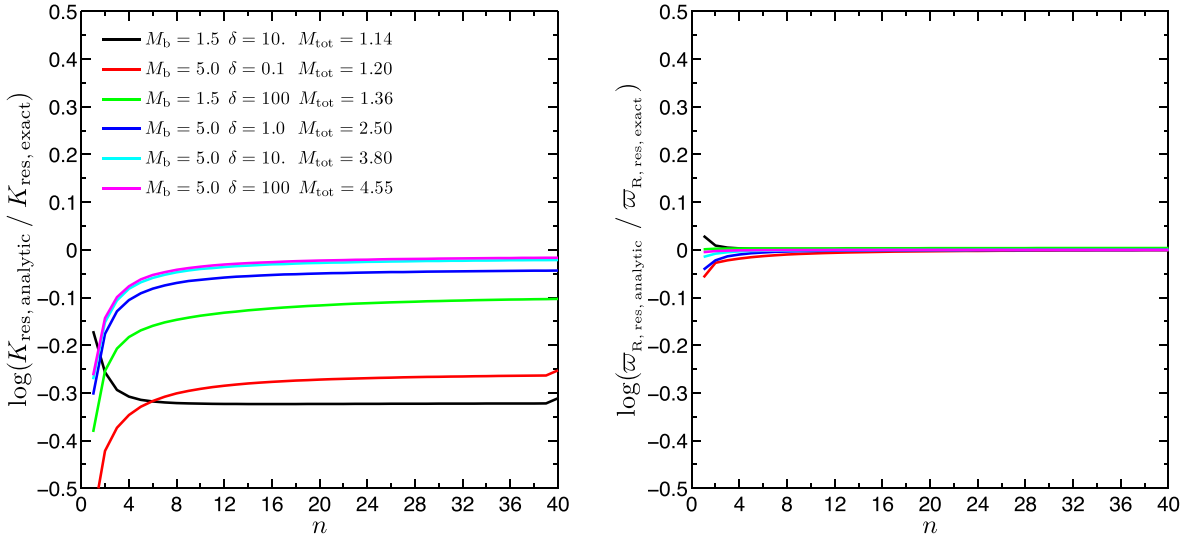

Figure H1. Comparison of our analytic estimate for the resonant wavenumber, K_{res} (equation H9, left), and the real part of the resonant phase velocity, $\varpi_{R,\,res}$ (equation H4a, right), to a numerical solution of the dispersion relation. We compare the first 40 modes, $n = 1$–40, for the same values of M_b and δ as in Fig. F1. The approximation for K_{res} is poor when $M_{tot} \lesssim 1.3$, but for $M_{tot} \gtrsim 2$ the error is less than ∼10 per cent for $n > 4$. On the other hand, the approximation for $\varpi_{R,\,res}$ is very good even at low Mach numbers.

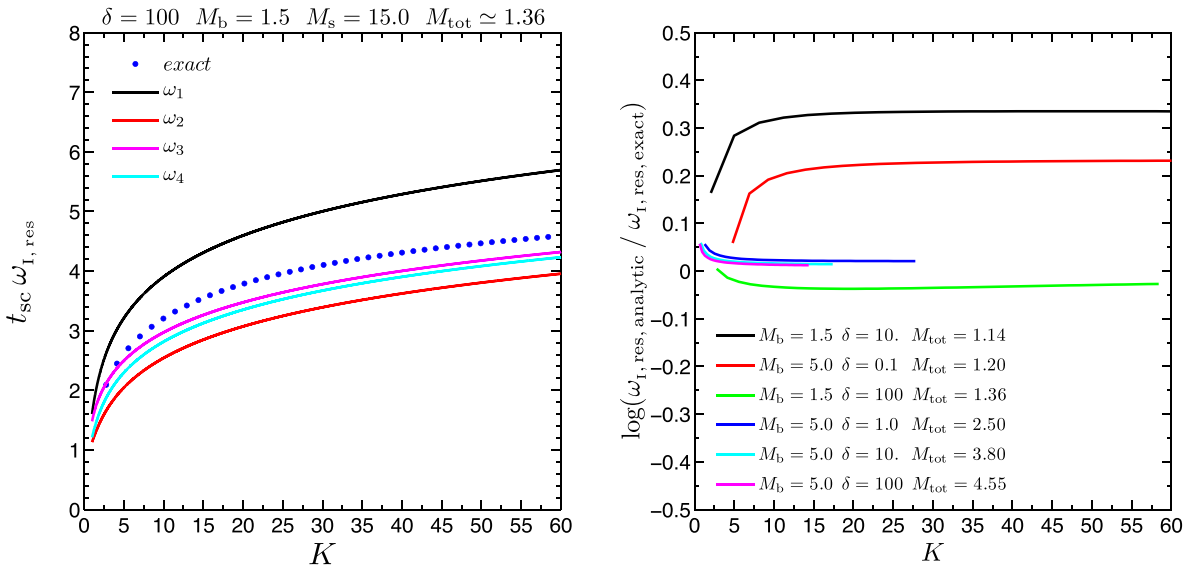

Figure H2. Analytic estimate versus numerical solutions for the fastest growing mode in the slab. Left: comparison of the growth rate at resonance, $\omega_{I,\,res}$, computed numerically for the first 40 modes (blue points) and calculated analytically using the first four terms in the sequence in equation (H8) (solid lines), for $M_b = 1.5$ and $\delta = 100$. The analytic series converges by $\omega_{I,\,3}$, though in this case it converges to a slightly lower value than the numerical solution. Right: the ratio of $\omega_{I,\,3}$ from equation (H8) to the numerical solution for the same values of M_b and δ as in Fig. H1. Note that the wavenumber corresponding to $n = 40$ is different in each case, which is why different curves end at different K values. The fit is quite poor for $M_{tot} \lesssim 1.3$, but for higher Mach numbers the error is less than 10 per cent.

This paper has been typeset from a TEX/LATEX file prepared by the author.